Journal of
Marine Science and Engineering

MDPI

Article

Global Path Planning for UUVs in Nearshore Environments Using an IAPF-RRT* Method

Xiaojing Fan [1,2], Fang Kong [2], Zhenhao Cui [3] and Yinjing Guo [3,*]

1 School of Physics and Electronic Information, Weifang University, Weifang 261061, China; xiaojingfan@wfu.edu.cn
2 College of Electrical Engineering and Automation, Shandong University of Science and Technology, Qingdao 266590, China; 202181080004@sdust.edu.cn
3 College of Electronic and Information Engineering, Shandong University of Science and Technology, Qingdao 266590, China; zhenhcui@126.com
* Correspondence: gyjlwh004@126.com

Abstract

Nearshore environments, characterized by complex obstacle distributions and dynamic disturbances, pose significant challenges to global path planning for unmanned underwater vehicles (UUVs). To address these challenges, this paper proposes an improved artificial potential field-guided RRT* (IAPF-RRT*) method for efficient and robust path planning in coastal environments. The proposed approach integrates an improved artificial potential field into the sampling and node expansion processes to enhance goal-directed exploration and obstacle avoidance capability. In addition, a target-biased sampling strategy and an adaptive attraction mechanism are introduced to accelerate convergence, while a NURBS-based refinement scheme is employed to improve trajectory continuity and smoothness. Extensive simulations in representative scenarios demonstrate that the proposed method significantly improves planning efficiency, reducing planning time by up to 80% compared with conventional RRT-based methods, while substantially decreasing redundant node expansion and improving trajectory smoothness. A consistently high success rate is maintained across all scenarios. Field experiments in nearshore environments further validate the robustness and practical applicability of the proposed method. These results indicate that the proposed IAPF-RRT* method achieves a favorable balance between efficiency, robustness, and path quality, making it well-suited for real-world UUV operations in complex nearshore environments.

Keywords: unmanned underwater vehicles (UUVs); global path planning; nearshore environments; RRT*; artificial potential field; autonomous navigation

Check for updates

Academic Editor: Jinfen Zhang

Received: 2 April 2026
Revised: 26 April 2026
Accepted: 29 April 2026
Published: 30 April 2026

Copyright: © 2026 by the authors. Licensee MDPI, Basel, Switzerland. This article is an open access article distributed under the terms and conditions of the Creative Commons Attribution (CC BY) license.

1. Introduction

With the increasing demand for marine resource exploitation and sustainable ocean management, activities such as coastal exploration [1], environmental monitoring [2], seabed mapping [3], and military reconnaissance [4] have become increasingly important. These tasks are typically conducted in nearshore and shallow-water environments, which are characterized by complex and highly heterogeneous conditions. In such environments, autonomous navigation is particularly challenging due to dense obstacle distributions, limited maneuvering space, and dynamic disturbances induced by ocean currents and tidal effects. Unmanned Underwater Vehicles (UUVs), capable of autonomous operation in complex underwater environments, have gradually become indispensable tools for scientific investigation and environmental monitoring in coastal regions. Equipped with task-specific sensing systems, UUVs can perform real-time measurements of key environmental parameters, including temperature, salinity, turbidity, and dissolved oxygen [5], while autonomous navigation significantly improves operational efficiency, safety, and mission reliability.

Path planning plays a central role in UUV autonomous navigation. It aims to generate a safe, feasible, and collision-free trajectory from the start point to a target location while optimizing performance metrics such as path length, energy consumption, and travel time [6]. However, nearshore environments introduce significant challenges due to irregular seabed topography, dense static obstacles, and dynamic disturbances. For example, in aquaculture scenarios, UUVs must avoid fixed structures such as cages and reefs while responding to moving objects such as vessels and marine organisms. These factors make it difficult for conventional planning methods to simultaneously achieve high efficiency, robustness, and solution optimality.

Existing path-planning approaches can generally be categorized into global and local methods [6,7]. From a methodological perspective, they can be further divided into graph search-based, artificial potential field (APF)-based, bio-inspired optimization, and sampling-based approaches. Graph search methods, such as A* and Dijkstra algorithms [8–10], guarantee completeness and can obtain optimal solutions in discretized environments. Their computational complexity increases significantly with the size and resolution of the environment, which limits their applicability in large-scale and continuous underwater scenarios. APF-based methods have been widely applied in AUV/UUV path-planning due to their high computational efficiency and intuitive physical interpretation. The classical formulation proposed by Khatib [11] enables real-time obstacle avoidance through artificial attractive and repulsive forces. Subsequent studies have extended this framework to underwater environments, including improved APF formulations for AUV path planning [12], multisource data-assisted potential field modeling [13], dynamic velocity-based potential field methods for multi-AUV coordination [14], and grid-based APF fusion strategies for handling complex obstacle distributions [15]. Despite these improvements, APF-based methods still suffer from inherent limitations, such as local minima, oscillatory behavior, and target non-reachability, which restrict their reliability in complex environments. To further address these limitations, recent studies have explored advanced APF-based approaches by incorporating bio-inspired and learning-based mechanisms. For example, membrane evolutionary artificial potential field methods introduce evolutionary strategies to enhance global search capability and alleviate local minima issues [16]. In addition, QAPF-based learning approaches integrate adaptive learning mechanisms to improve path planning performance in both known and unknown environments [17]. However, these methods still primarily rely on potential-field formulations and lack an effective global exploration capability. As a result, their performance remains limited in complex environments with highly constrained spaces or dynamic obstacles. Bio-inspired optimization methods, such as ant colony optimization and genetic algorithms, have also been explored for underwater path planning. For instance, improved ant colony algorithms have been used to generate smooth AUV trajectories [18,19], while adaptive genetic algorithms have been applied to dynamic 3D path planning [20]. In addition, recent studies have incorporated environmental factors such as ocean currents [21] and hydrodynamic effects through CFD-assisted optimization frameworks [22], further enhancing path feasibility. These methods provide strong global search capability and flexibility. They typically involve high computational cost and iterative optimization processes, making real-time implementation challenging in dynamic underwater environments. Sampling-based methods, particularly RRT and its variants, have attracted increasing attention due to their probabilistic completeness and ability to efficiently explore high-dimensional spaces. Compared with graph search and optimization-based approaches, these methods exhibit better adaptability to complex and continuous environments. However, their reliance on stochastic sampling often leads to slow convergence and redundant node expansion, especially in cluttered scenarios. While each category offers distinct advantages, none of them can simultaneously achieve efficient global exploration and reliable local guidance in complex underwater environments, which motivates the development of more effective hybrid planning frameworks.

Among sampling-based approaches, the Rapidly exploring Random Tree (RRT) [23] algorithm has been widely applied to underwater navigation problems due to its probabilistic completeness and wide application in underwater applications [24,25]. To address its lack of optimality, Karaman and Frazzoli [26] introduced the RRT* algorithm, which achieves asymptotic optimality through a rewiring mechanism based on random geometric graphs. As the number of iterations approaches infinity, RRT* is guaranteed to converge to the optimal solution. This property makes RRT* more suitable for long-duration and energy-constrained UUV missions [6,27]. To improve the sampling efficiency of RRT*, Gammell et al. [28] proposed the Informed-RRT* algorithm. This method first obtains an initial feasible solution using RRT*, and then restricts subsequent sampling to an ellipsoidal subset of the state space defined by the start, goal, and current path cost. As the solution is iteratively refined, the sampling region progressively shrinks, thereby accelerating convergence toward the optimal solution [29]. Despite its asymptotic optimality, RRT* often suffers from slow convergence due to its single-tree exploration mechanism. To address this limitation, bidirectional search strategies have been introduced. The bidirectional RRT* (Bi-RRT*) [30] algorithm accelerates convergence by simultaneously growing two trees from the start and goal states, thereby reducing redundant exploration and improving search efficiency. This strategy has also been applied in underwater path planning scenarios [31]. More recently, RRT*-based approaches have been further developed for long-horizon and cost-aware path planning to improve trajectory efficiency in extended missions [32], as well as curvature-constrained trajectory generation using B-spline representations to ensure smoothness and kinematic feasibility [33].

In recent years, state-of-the-art (SOTA) path-planning methods have increasingly focused on enhancing RRT*-based frameworks through heuristic guidance and structural optimization. Representative approaches include Informed-RRT*, bidirectional RRT*-based methods, and hybrid APF-guided RRT* frameworks, which introduce directional guidance into the sampling and node-expansion processes to improve convergence efficiency and path quality. To further improve search efficiency, heuristic guidance mechanisms have been introduced to bias sampling toward target regions, improving goal-oriented search behavior [34]. Building on this idea, artificial potential field (APF)-based guidance has been incorporated into RRT frameworks to further enhance exploration efficiency [35]. Hybrid APF-RRT and APF-RRT* methods have been proposed to improve exploration efficiency [36–38], where potential field guidance is incorporated into the sampling and node expansion processes. Moreover, adaptive potential functions and enhanced sampling strategies have been proposed to further improve robustness and planning efficiency [39].

Despite these advances, most existing SOTA methods rely on heuristic-level integration, where guidance strategies are applied as external bias terms without modifying the underlying tree-growth mechanism. As a result, the interaction between global exploration and local guidance remains loosely coupled, limiting their ability to effectively resolve issues such as local minima, target non-reachability, and dynamic adaptability in complex environments. To provide a clear understanding of the characteristics of existing methods, a comparative summary of representative path-planning approaches is presented in Table 1.

Table 1. Functional capability comparison of representative path-planning methods.

Algorithm	Global Exploration	Directed Guidance	Fast Convergence	Local Minima Avoidance	Goal Reachability	Dynamic Obstacle Handling	Path Smoothness
APF	×	✓	✓	×	×	△	△
RRT	✓	×	△	✓	✓	×	×
RRT*	✓	×	×	✓	✓	×	△
Bi-RRT*	✓	×	✓	✓	✓	×	△
Informed-RRT*	✓	△	△	✓	✓	×	△
APF-RRT*	✓	✓	△	×	×	△	△
Bi-APF-RRT*	✓	✓	✓	×	×	△	△
Our IAPF-RRT*	✓	✓	✓	✓	✓	✓	✓

✓ indicates the feature is supported, × indicates the feature is not supported, △ denotes partially supported.

As shown in Table 1, different methods exhibit complementary strengths but also inherent limitations. APF-based methods provide efficient local guidance and strong directionality, but they lack global exploration capability and are prone to local minima and target non-reachability. In contrast, RRT-based methods ensure reliable global exploration and asymptotic optimality, but suffer from low convergence efficiency and redundant node expansion due to their inherent randomness. Hybrid APF-RRT* approaches attempt to combine these advantages, but their performance remains constrained in complex and dynamic environments. SOTA path-planning methods primarily focus on improving sampling-based frameworks through enhanced exploration strategies, heuristic guidance, and hybrid integrations, such as Informed-RRT*, bidirectional RRT*-based methods, and APF-guided RRT* variants. Despite these advances, most existing methods rely on loosely coupled integration strategies, where guidance mechanisms are introduced as external heuristic biases without fundamentally modifying the underlying tree-growth process. As a result, the coordination between global exploration and local guidance remains suboptimal, limiting their ability to effectively address challenges such as local minima, target non-reachability, and dynamic obstacle interactions. There is still a need for a more tightly integrated planning framework that can simultaneously enhance exploration efficiency and guidance reliability. This motivates the development of the proposed method.

To address these limitations, this paper proposes an Improved Artificial Potential Field-guided RRT* (IAPF-RRT*) framework for global path planning in nearshore environments. Unlike conventional approaches, the proposed method introduces a mechanism-level integration of the potential field into the tree expansion process. Specifically, the IAPF is designed to explicitly mitigate local minima, ensure target reachability, and incorporate dynamic obstacle interactions. Furthermore, the potential field is embedded into both the sampling and node-expansion stages, enabling a tightly coupled interaction between stochastic exploration and directional guidance. This results in improved convergence efficiency, enhanced path quality, and stronger robustness in complex environments.

The primary contributions of this paper are summarized as follows:

1. An improved artificial potential field-guided RRT* (IAPF-RRT*) framework is proposed, in which the potential field is tightly integrated into the sampling and node expansion processes. This mechanism-level integration enhances the coupling between stochastic exploration and directional guidance, thereby improving goal-directed search and obstacle avoidance capability.
2. A target-biased sampling strategy and a weight-adaptive attraction mechanism are developed to balance global exploration and local exploitation. These strategies accelerate convergence and effectively reduce redundant node expansion, leading to improved planning efficiency.

3. A NURBS-based path refinement scheme is introduced to improve trajectory continuity and curvature smoothness. This post-processing approach generates higher-quality and dynamically feasible paths for UUV operations.
4. Extensive simulations and real-world field experiments in representative nearshore environments are conducted to validate the proposed method. The results demonstrate significant improvements in planning efficiency, path quality, and robustness compared with state-of-the-art RRT-based methods, confirming the practical applicability of the framework.

The remainder of this paper is organized as follows: Section 2 introduces the problem formulation and the necessary background. Section 3 presents the proposed IAPF-RRT* framework. Section 4 reports the results from both simulation and field experiments and provides a comprehensive discussion. Section 5 concludes the paper.

2. Mathematical Representation

This section briefly reviews the RRT* algorithm and the APF method, followed by a discussion of their limitations to motivate the proposed approach.

2.1. Problem Formulation

In this study, the global path planning problem for a UUV operating in nearshore environments is formulated in a continuous configuration space. Let q_{init} and q_{goal} denote the initial and target states, respectively. The objective is to generate a collision-free and dynamically feasible trajectory that connects the start and goal while optimizing path quality metrics such as length, smoothness, and safety.

The environment consists of both static and dynamic obstacles. Static obstacles represent seabed structures such as reefs and aquaculture facilities, whereas dynamic obstacles include moving vessels and marine organisms. The path-planning algorithm must therefore ensure collision avoidance under both geometric and kinematic constraints.

2.2. RRT Algorithm*

The RRT* algorithm is a sampling-based motion planning method that incrementally constructs a tree in the collision-free configuration space to explore feasible paths while optimizing path quality. As shown in Figure 1, starting from the initial state q_{init}, the algorithm iteratively samples random states q_{rand} from the free space and identifies the nearest node $q_{nearest}$ in the current tree according to a distance metric. A new node q_{new} is then generated by steering from $q_{nearest}$ toward q_{rand} with a predefined step size Δd, provided that the motion is collision-free. Unlike the standard RRT algorithm, RRT* introduces an optimization mechanism through a neighborhood search and rewiring process. Specifically, a set of neighboring nodes Q_{near} within a certain radius around q_{new} is identified. Among these candidates, the node that yields the minimum cost from the start state to q_{new} is selected as its parent. Subsequently, the algorithm evaluates whether the newly added node q_{new} can serve as a better parent for nearby nodes. If a lower-cost path is found, the tree structure is updated accordingly. This process of sampling, node expansion, and local rewiring is repeated until the tree reaches the goal region or satisfies a predefined termination condition. Finally, the optimal path is obtained by tracing back from the goal node to the initial state along the parent links in the tree.

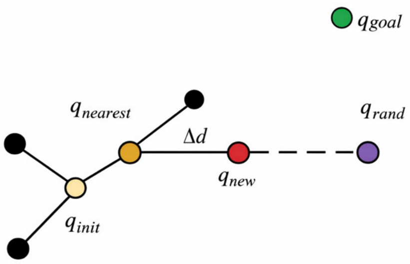

Figure 1. RRT* sampling illustration.

2.3. APF Algorithm

The APF method models the UUV as a particle moving under the combined influence of attractive and repulsive potential fields. The attractive potential is generated by the target, while repulsive potentials are induced by surrounding obstacles [11]. The motion of the UUV is governed by the resultant force derived from the gradient of the total potential field, as illustrated in Figure 2.

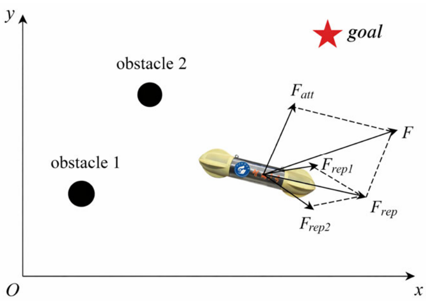

Figure 2. The combined force analysis of UUV.

Figure 2 shows that the UUV is subject to an attractive force F_{att} from the goal as well as repulsive components F_{rep1}, F_{rep2} generated by nearby obstacles. The resultant force F acting on the UUV is obtained through vector superposition. The UUV trajectory follows the direction of the steepest descent of the potential field, which is governed by the negative gradient of the total potential.

Attractive potential field. Let $q(x, y, z)$ denote the UUV position and $q_g(x_g, y_g, z_g)$ denote the target position. The attractive potential field U_{att} is defined as follows:

$$U_{att} = \frac{1}{2} k_{att} \rho^2(q, q_g) \tag{1}$$

where k_{att} is the proportional gain coefficient parameter, while $\rho(q, q_g)$ is the Euclidean distance between the UUV and the target.

$$\rho(q, q_g) = \|q, q_g\| = \sqrt{(x - x_g)^2 + (y - y_g)^2} \tag{2}$$

The corresponding attractive force $F_{att}(q)$ is the negative gradient of the potential field $U_{att}(q)$. It always points from the UUV toward the target, and its magnitude increases with distance.

$$F_{att}(q) = -\nabla U_{att}(q) = -\nabla(\frac{1}{2} k_{att} \rho^2(q, q_g)) = -k_{att} \rho(q, q_g) \tag{3}$$

Repulsive potential field. The repulsive potential field $U_{rep}(q)$ generated by an environmental obstacle is defined as follows:

$$U_{rep}(q) = \begin{cases} \frac{1}{2}k_{rep}(\frac{1}{\rho(q,q_o)} - \frac{1}{\rho_o})^2 & 0 \leq \rho(q,q_o) \leq \rho_o \\ 0 & \rho(q,q_o) > \rho_o \end{cases} \tag{4}$$

where k_{rep} is the proportional gain coefficient, q_o denotes the obstacle position, and $\rho(q,q_o)$ represents the Euclidean distance between the obstacle and the UUV. The parameter ρ_o is the maximum influence range. The distance $\rho(q,q_o)$ is expressed as follows:

$$\rho(q,q_o) = \|q,q_o\| = \sqrt{(x-x_o)^2 + (y-y_o)^2} \tag{5}$$

within the obstacle influence region, the repulsive force $F_{rep}(q)$ is obtained as the negative gradient of $U_{rep}(q)$.

$$F_{rep}(q) = \begin{cases} k_{rep}(\frac{1}{\rho(q,q_o)} - \frac{1}{\rho_o})\frac{1}{\rho^2(q,q_o)}\nabla\rho(q,q_o) & 0 \leq \rho(q,q_o) \leq \rho_o \\ 0 & \rho(q,q_o) > \rho_o \end{cases} \tag{6}$$

where the unit direction vector $\nabla\rho(q,q_o)$ from the obstacle to the UUV is expressed as follows:

$$\nabla\rho(q,q_o) = \frac{q-q_o}{|q-q_o|} \tag{7}$$

The repulsive force increases rapidly as the UUV approaches the obstacle, ensuring collision avoidance.

Total potential field. The total artificial potential field $U(q)$ is obtained by superimposing the attractive potential field $U_{att}(q)$ and the repulsive potential fields $U_{rep,i}(q)$.

$$U(q) = U_{att}(q) + \sum_{i=1}^{n} U_{rep,i}(q) \tag{8}$$

Here, n denotes the number of obstacles.

The resultant force $F(q)$ acting on the UUV is defined as the negative gradient of the total potential field.

$$F(q) = -\nabla U(q) = F_{att}(q) + \sum_{i=1}^{n} F_{rep,i}(q) \tag{9}$$

Under the action of the total potential field, the UUV moves from regions of higher potential toward lower potential, gradually approaching the target while maintaining safe distances from obstacles. This process corresponds to a gradient-descent-based path generation mechanism in the configuration space.

In addition to sampling-based methods, optimization-based approaches such as CHOMP and TrajOpt have demonstrated strong performance in structured environments by directly optimizing trajectory smoothness and feasibility. Meanwhile, learning-based approaches, including reinforcement learning and deep neural networks, have shown promising adaptability in complex and dynamic scenarios.

However, the application of these methods in nearshore UUV environments remains challenging due to environmental uncertainty, limited prior information, and high computational requirements. In contrast, sampling-based methods provide a favorable balance between computational efficiency, robustness, and real-time applicability. Therefore, this work focuses on improving sampling-based planning through adaptive guidance mechanisms.

3. IAPF-RRT*-Based Path-Planning Framework

In this section, the proposed IAPF-RRT* algorithm is presented to address the limitations of conventional RRT*-based methods, where IAPF is incorporated to guide sampling and improve exploration efficiency.

3.1. Overview

The proposed IAPF-RRT* integrates the complementary advantages of the IAPF and RRT* methods, where the potential-field forces generated by the IAPF are embedded into the random-sampling and node-expansion processes to provide dynamic guidance during tree growth. Figure 3 illustrates the overall structure of the proposed method. First, an IAPF-based guidance strategy is incorporated into the sampling and node-expansion processes, enabling the random tree to grow toward promising regions while improving goal-directed exploration. Second, a sampling-bias mechanism is introduced to steer the sampling process toward the target region, thereby enhancing convergence efficiency and reducing unnecessary exploration. Third, a weight-adaptive attraction guidance mechanism is designed to regulate node expansion, effectively suppressing redundant branch growth while maintaining efficient tree extension toward the goal. Finally, a path refinement module is employed to improve trajectory quality. Redundant nodes are removed through post-processing, and NURBS-based interpolation is applied to enhance path smoothness and curvature continuity, thereby improving maneuverability in confined coastal environments. The detailed implementation of these components is presented in the following subsections.

3.2. Improved Artificial Potential Field (IAPF) Strategy

Although RRT* alleviates local-minimum stagnation through stochastic exploration, an IAPF is still required to enhance local robustness, address target non-reachability, and ensure safe navigation in dynamic environments. To overcome the target non-reachability issue in conventional APF, a distance-adjusted repulsive potential is introduced to guarantee that the goal remains the global minimum of the potential field. To resolve local minima, a virtual sub-goal escape strategy is designed to break the force equilibrium between the target attraction and obstacle repulsion. Furthermore, to handle dynamic obstacles, a relative-velocity-based avoidance mechanism is incorporated to enable adaptive path adjustment in the presence of moving objects. These improvements significantly enhance the robustness and adaptability of UUV path planning in highly dynamic coastal environments. The workflow of the proposed IAPF process is illustrated in Figure 4.

3.2.1. Goal Non-Reachability Mitigation Strategy

To overcome the goal non-reachability problem, the proposed IAPF method introduces a distance-adjusted repulsive potential formulation. The repulsive potential field function U^*_{rep} is modified by introducing the distance $\rho(q, q_g)$ between the UUV and the target point, together with a repulsive correction factor n. This function adaptively adjusts the repulsive potential field strength according to the UUV target distance, thereby ensuring that the repulsive potential decays as the goal is approached. As a result, the target consistently remains the global minimum of the potential field.

In accordance with the practical requirements of UUV path planning, the mathematical expression of $U^*_{rep}(q)$ can be formulated as follows:

$$U^*_{rep}(q) = \begin{cases} \frac{1}{2}k_{rep}(\frac{1}{\rho(q,q_o)} - \frac{1}{\rho_o})^2\rho^n(q,q_g) & 0 \leq \rho(q,q_o) \leq \rho_o \\ 0 & \rho(q,q_o) > \rho_o \end{cases} \quad (10)$$

In contrast to the conventional repulsive potential in Equation (4), the modified formulation in Equation (10) adjusts the repulsive field strength based on the distance $\rho(q, q_o)$ and the repulsive correction factor n, thereby preserving the target as the global minimum of the potential landscape. Furthermore, the repulsive component becomes zero when the UUV-obstacle distance exceeds the maximum influence range of the repulsive field (i.e., $\rho(q, q_o) > \rho_o$).

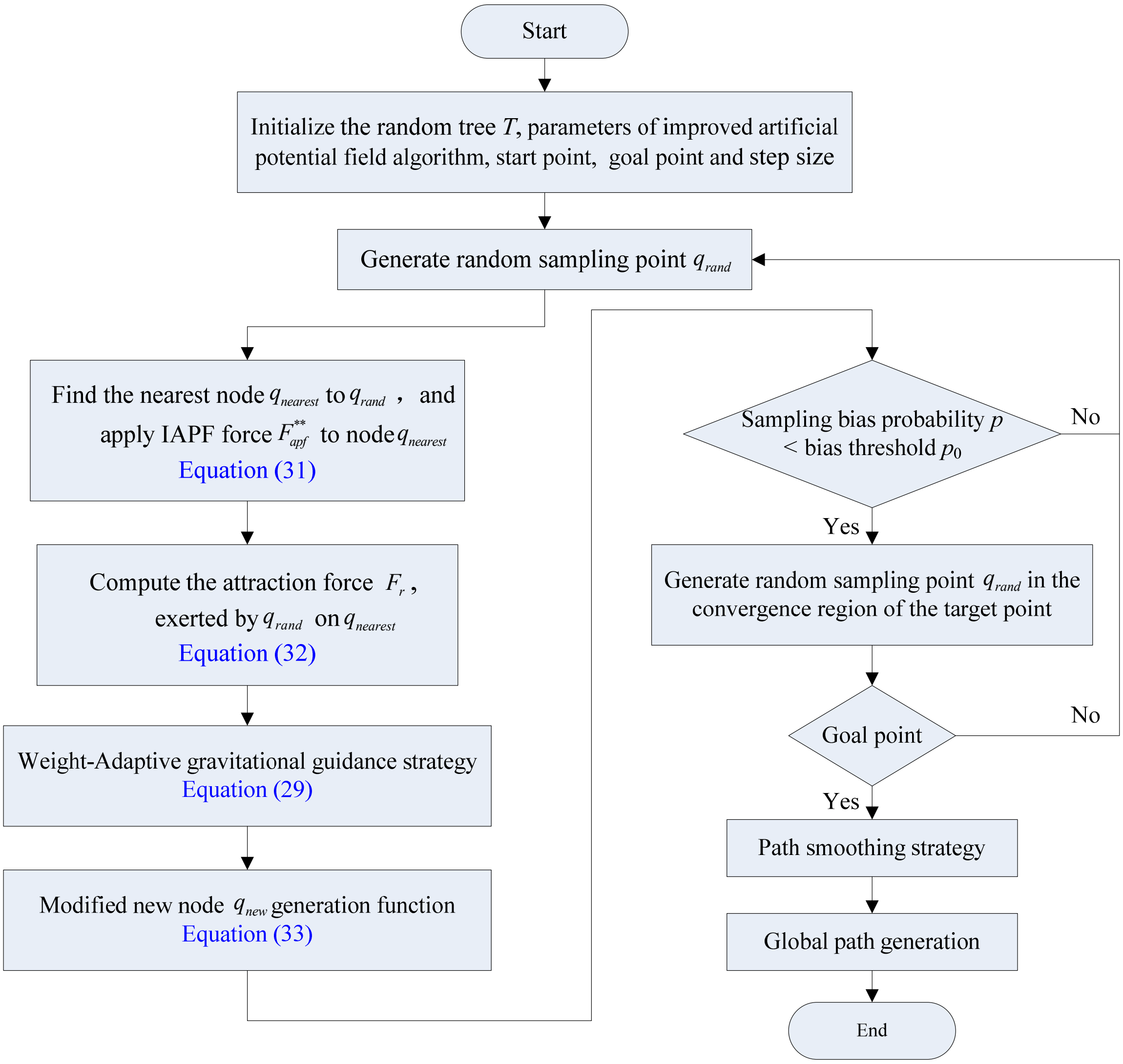

Figure 3. IAPF-RRT algorithm flowchart.

As the vehicle moves closer to the goal, the magnitude of the corrected repulsive potential field gradually diminishes in proportion to the remaining distance between the UUV and the target. The repulsion correction factor n serves to regulate the decay rate of the repulsive potential field. When n = 0, the corrected repulsive potential field $U_{rep}^*(q)$ is identical to the original repulsive potential field $U_{rep}(q)$, and no modification is applied. When n is a positive constant, the repulsive force decays to zero as the UUV approaches the goal. The selection of the parameter n is critical: an excessively large value can compromise obstacle avoidance. Consequently, n should be initialized with a small value and increased gradually to achieve effective regulation of the repulsive potential field.

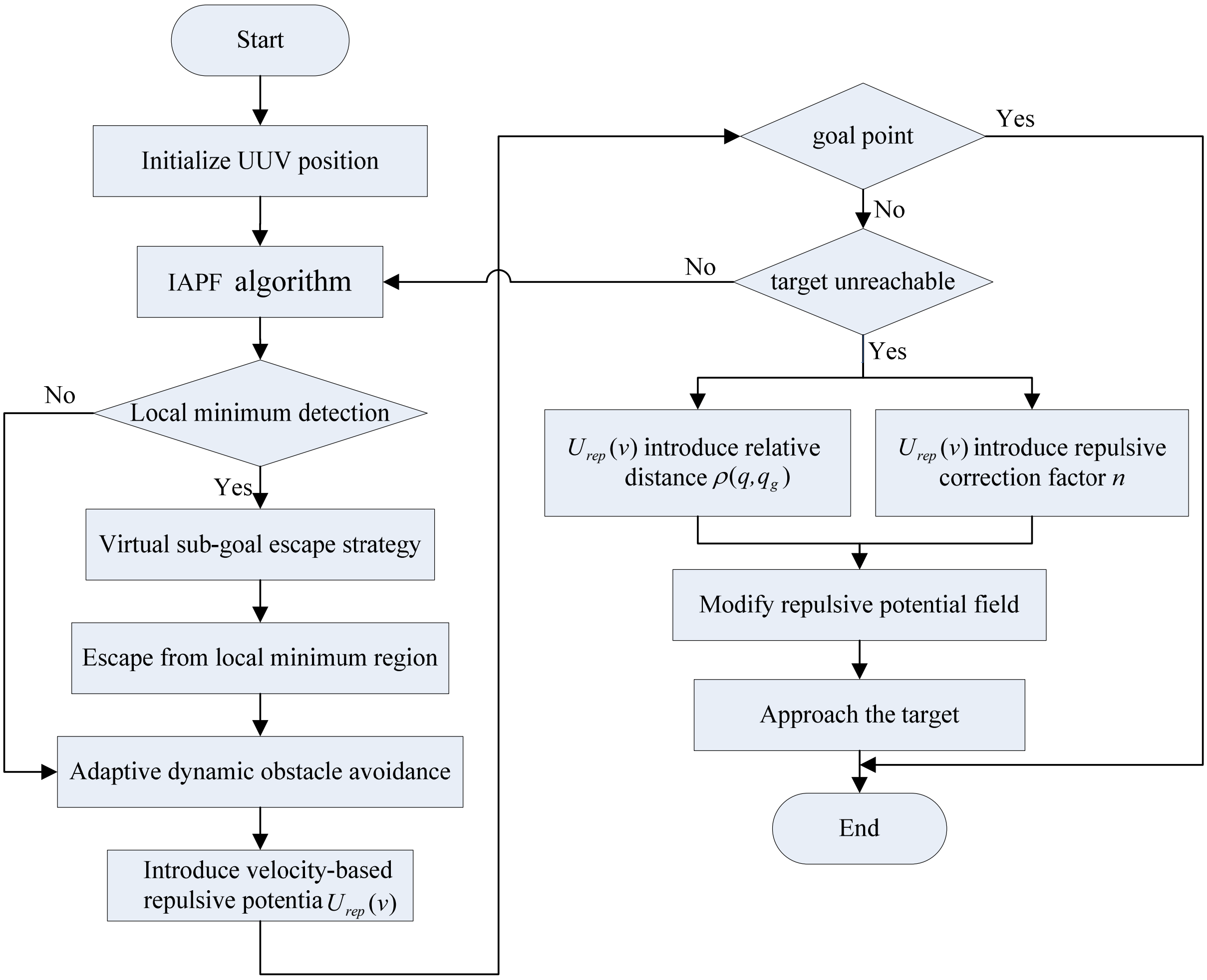

Figure 4. Flowchart of the IAPF Algorithm.

When the UUV enters the influence range of the corrected repulsive potential field, the corrected repulsive force $F^*_{rep}(q)$ is defined as the negative gradient of the corrected repulsive potential field function $U^*_{rep}(q)$.

$$F^*_{rep}(q) = -\nabla U^*_{rep}(q) = \begin{cases} F^*_{rep1}(q) + F^*_{rep2}(q) & 0 \le \rho(q, q_o) \le \rho_o \\ 0 & \rho(q, q_o) > \rho_o \end{cases} \tag{11}$$

The corrected repulsive force consists of two components, $F^*_{rep1}(q)$ and $F^*_{rep2}(q)$, whose mathematical expressions are provided in Equations (12) and (13), respectively.

$$F^*_{rep1}(q) = k_{rep}\left(\frac{1}{\rho(q, q_o)} - \frac{1}{\rho_o}\right)\frac{1}{\rho^2(q, q_o)}\nabla\rho(q, q_o)\rho^n(q, q_g) \tag{12}$$

$$F^*_{rep2}(q) = -\frac{n}{2}k_{rep}\left(\frac{1}{\rho(q, q_o)} - \frac{1}{\rho_o}\right)^2 \rho^{n-1}(q, q_g)\nabla\rho(q, q_g) \tag{13}$$

The component $F^*_{rep1}(q)$ is determined by $\nabla\rho(q, q_g)$ and is directed from the obstacle toward the UUV, while the component $F^*_{rep2}(q)$ is determined by $\nabla\rho(q, q_g)$ and points from the UUV toward the target. In the IAPF algorithm, the corrected repulsive field is analyzed vectorially, as illustrated in Figure 5. The corrected repulsive force depends not only on the distance between the UUV and the obstacle but also gradually weakens as the UUV approaches the target, with the decay rate regulated by the correction factor n. When the UUV approaches the goal region, the repulsive effect becomes much weaker, which enables the resultant force F^* to better align with the desired direction and ultimately eliminates the target non-reachability issue.

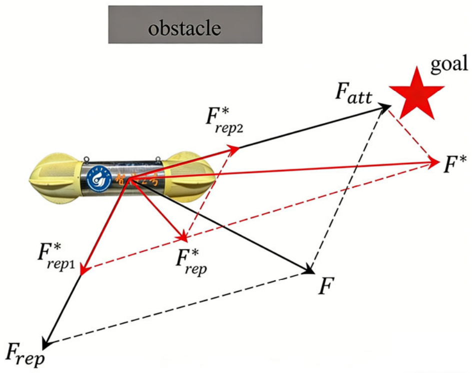

Figure 5. Vector analysis diagram of IAPF correction repulsive potential field.

When $n = 0$, the corrected force component $F^*_{rep2}(q)$ becomes zero, and the corrected repulsive force $F^*_{rep}(q)$ degenerates into the original repulsive force $F_{rep}(q)$. Under this condition, the repulsive field formulation reduces to the conventional artificial potential field, and the corrective mechanism is no longer active.

When $n > 0$, the corrected repulsive force component $F^*_{rep2}(q)$ becomes active and is adjusted according to the relative distance between the UUV and the target. Depending on the value of n, three representative cases can be identified.

1. For $0 < n < 1$, the corrected repulsive force $F^*_{rep}(q)$ becomes non-differentiable at the target point $x = x_g$. When the relative distance satisfies $\rho(q, q_o) < \rho_o$, the corrected repulsive force function is expressed as:

$$F^*_{rep1}(q) = k_{rep}(\frac{1}{\rho(q,q_o)} - \frac{1}{\rho_o})\frac{1}{\rho^2(q,q_o)}\rho^n(q,q_g) \tag{14}$$

$$F^*_{rep2}(q) = -\frac{n}{2}k_{rep}(\frac{1}{\rho(q,q_o)} - \frac{1}{\rho_o})^2\frac{1}{\rho^{1-n}(q,q_g)} \tag{15}$$

As the UUV moves closer to the target and $\rho(q, q_g) \to 0$, the corrected repulsive force component $F^*_{rep1}(q) \to 0$, while the corrected repulsive force component $F^*_{rep2}(q) \to \infty$. The resultant force acting on the UUV remains positive and directed from the UUV toward the target, ensuring that the UUV can smoothly converge to its destination.

2. When $n = 1$, the separation between the UUV and the obstacle meets the condition $\rho(q, q_o) < \rho_o$, the corrected repulsive force can be expressed as:

$$F^*_{rep1}(q) = k_{rep}(\frac{1}{\rho(q,q_o)} - \frac{1}{\rho_o})\frac{1}{\rho^2(q,q_o)}\rho(q,q_g) \tag{16}$$

$$F^*_{rep2}(q) = -\frac{1}{2}k_{rep}(\frac{1}{\rho(q,q_o)} - \frac{1}{\rho_o})^2 \tag{17}$$

As the UUV gradually approaches the target point and $\rho(q, q_g) \to 0$, the corrected repulsive force component $F^*_{rep1}(q)$ tends toward zero, while the component $F^*_{rep2}(q)$ converges to a constant value. In this case, the overall corrected repulsive force $F^*_{rep}(q)$ asymptotically approaches $F^*_{rep2}(q)$. As a result, the combined force always directs the vehicle toward the destination, allowing it to maintain forward motion and ultimately arrive at the goal.

3. For $n > 1$, the corrected repulsive force $F^*_{rep}(q)$ is differentiable at the target point $x = x_g$. As the UUV moves closer to the goal and the relative distance $\rho(q, q_g)$ gradually decreases, the magnitude of the corrected repulsive force $F^*_{rep}(q)$ smoothly attenuates toward zero, allowing the resultant potential field to guide the UUV steadily toward the target.

3.2.2. Local Minimum Avoidance Strategy

To address the local minimum problem, a virtual sub-goal escape strategy is introduced. When the UUV becomes trapped in a local minimum region, the global target is temporarily replaced by a virtual sub-goal generated on the boundary of the obstacle's repulsive potential field. By reconfiguring the attractive potential field, the virtual sub-goal produces an escape force that disrupts the equilibrium between attractive and repulsive forces, guiding the UUV out of the local minimum region. Once the UUV reaches the virtual sub-goal, it is immediately deactivated, and the path-planning process resumes with the original global goal.

In the proposed IAPF algorithm, a circular region is constructed with the obstacle position as the center and the obstacle's repulsive influence range ρ_o as the radius. Tangent lines are drawn from both the current UUV position and the global goal position to this circle, yielding two tangent points. The virtual sub-goal is then defined as the midpoint of the circular arc between these two tangent points, as illustrated in Figure 6.

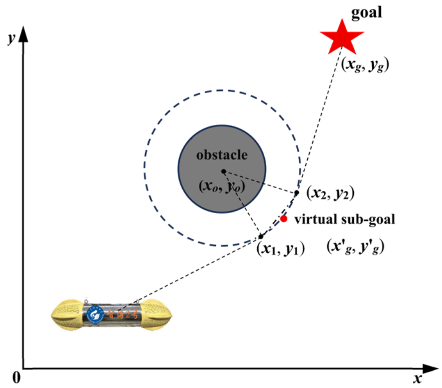

Figure 6. Build virtual sub-target points.

Let the current UUV position be denoted by (x, y), the obstacle center by (x_o, y_o), and the goal position by (x_g, y_g). The tangency point between the UUV and the constructed circle is denoted by (x_1, y_1), and the tangency point associated with the goal is denoted by (x_2, y_2). According to the geometric relationship, the tangency point (x_1, y_1) can be expressed as:

$$x_1 = x + \cos(\arctan\frac{y - y_o}{x - x_o} - \arcsin\frac{\rho}{\rho(q, q_o)}) \cdot \sqrt{\rho(q, q_o)^2 - \rho_o^2} \tag{18}$$

$$y_1 = y + \sin(\arctan\frac{y - y_o}{x - x_o} - \arcsin\frac{\rho_o}{\rho(q, q_o)}) \cdot \sqrt{\rho(q, q_o)^2 - \rho_o^2} \tag{19}$$

The coordinates of the tangency point (x_2, y_2) between the goal position and the circle can be expressed as:

$$x_2 = x_g + \sin(\arctan\frac{x_g - x_o}{y_g - y_o} - \arcsin\frac{\rho}{\rho(q_g, q_o)}) \cdot \sqrt{\rho(q_g, q_o)^2 - \rho_o^2} \tag{20}$$

$$y_2 = y_g - \cos(\arctan\frac{x_g - x_o}{y_g - y_o} - \arcsin\frac{\rho}{\rho(q_g, q_o)}) \cdot \sqrt{\rho(q_g, q_o)^2 - \rho_o^2} \tag{21}$$

The position coordinates of the virtual sub-goal are denoted by (x'_g, y'_g), which can be determined as:

$$x'_g = \frac{x_1 + x_2}{2} \tag{22}$$

$$y'_g = \frac{y_1 + y_2}{2} \tag{23}$$

3.2.3. Adaptive Dynamic Obstacle Avoidance Strategy

To address dynamic obstacle avoidance in complex environments, this paper proposes an adaptive obstacle avoidance strategy based on relative velocity analysis. The strategy builds upon the improved repulsive potential field model for solving the goal non-reachability problem and further incorporates obstacle velocity to construct a secondary corrected repulsive potential field U^{**}_{rep}. By analyzing the relative velocity between the UUV and dynamic obstacles along their line of sight, the proposed method determines whether the UUV is moving toward the obstacle. If the UUV is moving away from the dynamic obstacle, no avoidance action is required; if the UUV is moving toward the obstacle, the strategy is triggered to update the trajectory online, guaranteeing safe and reliable obstacle avoidance.

The mathematical expression of the secondary corrected repulsive potential field $U^{**}_{rep}(q, v)$ is defined as follows:

$$U^{**}_{rep}(q, v) = \begin{cases} U^{*}_{rep}(q) + U_{rep}(v) & 0 \le \rho(q, q_o) \le \rho_o \text{ and } v_{\dot{e}} \ge 0 \\ U^{*}_{rep}(q) & 0 \le \rho(q, q_o) \le \rho_o \text{ and } v_{\dot{e}} < 0 \\ 0 & else \end{cases} \tag{24}$$

The formulation of the repulsive potential component associated with relative velocity $U_{rep}(v)$ is given by

$$U_{rep}(v) = k_v \frac{(v - v_0)\dot{e}}{\rho(q, q_o)} = k_v \frac{v_{\dot{e}}}{\rho(q, q_o)} \tag{25}$$

In this formula, $U^{*}_{rep}(q)$ represents the corrected repulsive potential field defined in Equation (10), and $U_{rep}(v)$ denotes the velocity-based repulsive potential field of dynamic obstacles. The parameter k_v is the gain factor of the velocity repulsive potential field, v is the current velocity of the UUV, and v_0 represents the velocity associated with the obstacle. The term $v_{\dot{e}}$ denotes the relative velocity of the UUV with respect to the obstacle, projected along the line connecting them, while $\dot{e}$ is the unit direction vector along this line. When $v_{\dot{e}} \ge 0$, the UUV is moving toward the obstacle; when $v_{\dot{e}} < 0$, the UUV is moving away from it.

By taking the negative gradient of the secondary corrected repulsive potential field $U^{**}_{rep}(q, v)$, the velocity-aware secondary corrected repulsive force $F^{**}_{rep}(q, v)$ is obtained and can be expressed as follows:

$$F^{**}_{rep}(q, v) = -U^{**}_{rep}(q, v) = \begin{cases} F^{**}_{rep}(q) + F_{rep}(v) & 0 \le \rho(q, q_o) \le \rho_o \text{ and } v_{\dot{e}} \ge 0 \\ F^{*}_{rep}(q) & 0 \le \rho(q, q_o) \le \rho_o \text{ and } v_{\dot{e}} < 0 \\ 0 & else \end{cases} \tag{26}$$

The velocity repulsive force $F_{rep}(v)$ is expressed as

$$F_{rep}(v) = -\nabla U_{rep}(v) = -k_v \frac{(v - v_0)\dot{e}}{\rho(q, q_o)} = -k_v \frac{v_{\dot{e}}}{\rho(q, q_o)} \tag{27}$$

$F^*_{rep}(q)$ represents the corrected repulsive force defined in Equation (11), whereas $F_{rep}(v)$ denotes the velocity-based repulsive force induced by dynamic obstacles. When the UUV moves toward an obstacle, $F_{rep}(v)$ acts in the opposite direction, steering the vehicle away from the collision region. The vector analysis is illustrated in Figure 7a.

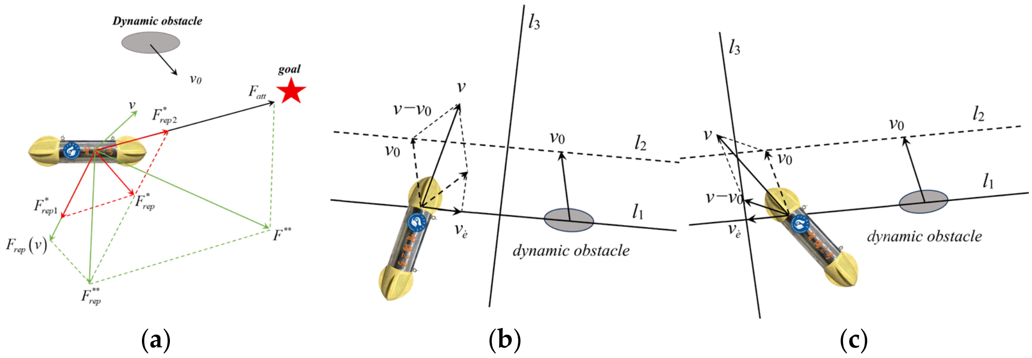

Figure 7. UUV and dynamic obstacle motion state: (**a**) repulsive potential field vector analysis; (**b**) $v_{\dot{e}} > 0$; (**c**) $v_{\dot{e}} < 0$.

The secondary corrected repulsive potential is further augmented by incorporating a velocity-dependent repulsive component associated with dynamic obstacles. This extension enhances the adaptability of the UUV in complex and time-varying environments, thereby improving navigation safety. By incorporating the relative motion information between the UUV and surrounding dynamic obstacles, a velocity vector $v_{\dot{e}}$ is introduced to characterize their relative motion state. This formulation enables the planner to distinguish between converging and diverging motion patterns, effectively preventing unnecessary or blind collision-avoidance maneuvers.

Figure 7b,c illustrate the relative motion configurations between the UUV and surrounding moving obstacles. In these illustrations, l_1 represents the line of sight between the UUV and the obstacle, with l_2 aligned along and l_3 orthogonal to it. In Figure 7b, when the UUV is heading toward the target ($v_{\dot{e}} \geq 0$), a dynamic obstacle avoidance maneuver needs to be executed. By contrast, in Figure 7c, when the UUV travels away from the obstacle ($v_{\dot{e}} < 0$), the relative motion itself increases the distance between them, so collision risk does not arise, and the velocity-based repulsive field does not need to intervene.

3.3. Target-Biased Sampling Strategy

Due to the inherent randomness of the sampling process, conventional RRT* may generate branches that deviate from the target region, leading to slow convergence. To address this issue, a target-biased sampling strategy is incorporated into the proposed IAPF-RRT* framework. A target convergence domain is defined based on the minimum distance R_g between the target q_{goal} and all obstacles. Specifically, the minimum distance R_g is used as the convergence radius to construct a circular collision-free region centered at the goal, as illustrated in Figure 8. This region represents a safe and effective convergence area for guiding tree expansion.

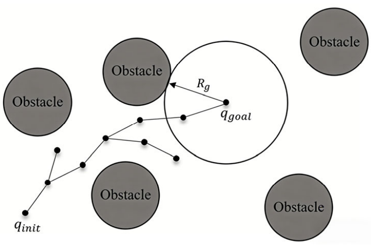

Figure 8. Target-Biased Sampling Strategy.

When the random tree enters the convergence region, a sampling bias mechanism is activated to steer the growth toward the goal. The rule generates a bias probability p to determine how sampling points are selected: if p is smaller than the preset threshold p_0, a random point is generated within the convergence region as the sampling point; otherwise, it is sampled from the global configuration space. By adjusting the probability of sampling within the target region, the proposed strategy effectively enhances goal-directed exploration and accelerates convergence. The sampling bias function is expressed in Equation (28).

$$q_{rand} = \begin{cases} GoalArea() & p \le p_0 \\ Sample() & otherwise \end{cases} \tag{28}$$

where *GoalArea*() generates samples within the convergence domain, and *Sample*() denotes global sampling, p_0 denotes the preset threshold, and q_{rand} represents the randomly generated sampling point.

3.4. Weight-Adaptive Attraction Strategy

To further enhance goal-directed tree expansion and suppress redundant node generation, a weight-adaptive attraction strategy is introduced into the IAPF-RRT* framework. When the nearest node $q_{nearest}$ lies within the artificial potential field formed by the target and surrounding obstacles, the IAPF generates an artificial potential force F_{apf}^{**} acting on $q_{nearest}$. This force is incorporated into the node expansion process to guide the generation of a new node q_{new}. The expansion direction of q_{new} is determined by a weighted combination of the attraction from the sampling point q_{rand} and the IAPF potential field, where the adaptive weights dynamically balance randomness and goal orientation. In this way, the tree grows in a more directed and efficient manner. The generation process of new nodes under this strategy is illustrated in Figure 9.

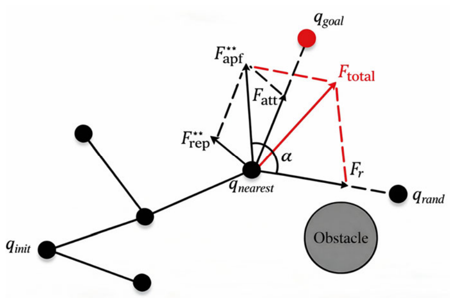

Figure 9. Weight adaptive gravity guidance strategy.

As shown in Figure 9, q_{init} and q_{goal} denote the start and target points, respectively, while q_{rand} represents the randomly sampled point and $q_{nearest}$ is the node nearest to q_{rand}. F_{rep}^{**} and F_{att} represent repulsive and attractive forces acting on $q_{nearest}$ under the improved potential field, whose resultant force is F_{apf}^{**}. Meanwhile, F_r indicates the attractive component from the sampled point on $q_{nearest}$. F_{total} denotes the combined force applied to the node $q_{nearest}$ under the attraction–guidance strategy, where α is the included angle between F_{apf}^{**} and F_r, with $\alpha \in [0, \pi]$.

The mathematical expression of the resultant force F_{total} is given by

$$F_{total}(q_{nearest}) = \lambda_1 F_{apf}^{**}(q_{nearest}) + \lambda_2 F_r(q_{nearest}) \tag{29}$$

where λ_1 denotes the weight of the IAPF force and λ_2 denotes the weight of the sampling point attraction; both λ_1 and λ_2 are defined as functions of the included angle α and satisfy $\lambda_1 + \lambda_2 = 1$.

$$\begin{aligned} \lambda_1 &= \sin^2 \alpha \\ \lambda_2 &= \cos^2 \alpha \end{aligned} \tag{30}$$

The weights λ_1 and λ_2 are dynamically adjusted based on the angle α between F_{apf}^{**} and F_r. When the forces are nearly perpendicular ($\alpha \to \pi/2$), the weight λ_1 approaches 1 and λ_2 approaches 0, promoting obstacle avoidance. Conversely, when they are nearly parallel ($\alpha \to 0$), the weight λ_2 approaches 1 and λ_1 approaches 0, reinforcing goal-directed expansion.

The resultant potential field force F_{apf}^{**} acting on $q_{nearest}$ under the influence of the artificial potential field is defined as follows:

$$F_{apf}^{**}(q_{nearest}) = F_{rep}^{**}(q_{nearest}) + F_{att}(q_{nearest}) \tag{31}$$

$F_{rep}^{**}(q_{nearest})$ is given in Equation (26) and $F_{att}(q_{nearest})$ is defined in Equation (3). The attractive force generated at the sampling point $q_{nearest}$ is defined as follows:

$$F_r(q_{nearest}) = \varepsilon \cdot \frac{q_{rand} - q_{nearest}}{\|q_{rand} - q_{nearest}\|} \vec{e_r} \tag{32}$$

ε denotes the random sampling gain factor, and $\vec{e_r}$ represents the unit vector from the nearest node to the sampling point. Considering the influence of the IAPF potential field on node generation, the IAPF-RRT* algorithm updates the position equation of the newly generated node $q_{nearest}$. The updated node generation formula is expressed as follows:

$$q_{new} = \begin{cases} q_{nearest} + \left(\frac{q_{rand} - q_{nearest}}{\|q_{rand} - q_{nearest}\|} + \frac{F_{apf}^{**}(q_{nearest})}{\left\|F_{apf}^{**}(q_{nearest})\right\|} \right) \times \Delta d & F_{apf}^{**}(q_{nearest}) \neq 0 \\ q_{nearest} + \left(\frac{q_{rand} - q_{nearest}}{\|q_{rand} - q_{nearest}\|} \right) \times \Delta d & F_{apf}^{**}(q_{nearest}) = 0 \end{cases} \tag{33}$$

3.5. Path Refinement Strategy

To reduce path length and suppress excessive turning, a path refinement strategy is introduced. First, redundant nodes in the sampled path are removed through an iterative loop-pruning process, thereby simplifying the path structure and improving computational efficiency. Subsequently, Non-Uniform Rational B-Spline (NURBS) interpolation is applied to the pruned path to generate a smooth trajectory with continuous curvature. This ensures a more natural and dynamically feasible path for UUV navigation.

The NURBS curve is employed to interpolate the remaining path nodes, thereby achieving smooth path optimization. The mathematical expression of the NURBS curve is given as follows:

$$C(u) = \frac{\sum_{i=0}^{n} N_{i,p}(u)\omega_i P_i}{\sum_{i=0}^{n} N_{i,p}(u)\omega_i} \tag{34}$$

$C(u)$ denotes the coordinates of a point on the NURBS curve, $N_{i,p}(u)$ denotes the i-th B-spline basis function of degree p in the parameter domain, ω_i is the weight factor, P_i is the control point. The end-point weights ω_0 and ω_n are positive, while the remaining weights ω_i satisfy the non-negative condition ($\omega_i \geq 0$). To avoid singularities or degeneration of the curve, it is required that any continuous weight factors cannot simultaneously be zero.

The zero-degree basis function ($p = 0$) is defined as follows:

$$N_{i,0}(u) = \begin{cases} 1 & u_i \leq u \leq u_{i+1} \\ 0 & Others \end{cases} \tag{35}$$

For higher-order basis functions ($p > 0$), the recursive definition is expressed as follows:

$$N_{i,p}(u) = \frac{u - u_i}{u_{i+p} - u_i} N_{i,p-1}(u) + \frac{u_{i+p+1} - u}{u_{i+p+1} - u_{i+1}} N_{i+1,p-1}(u) \tag{36}$$

The set of points is used as interpolation reference points. By performing inverse computation to determine the corresponding NURBS control points, the generated curve can maintain overall consistency with the UUV's actual trajectory. This approach ensures a continuous and smooth interpolation of the planned path, satisfying the UUV's requirements for smoothness, stability, and safety.

*3.6. Algorithm Description of IAPF-RRT**

In the proposed IAPF-RRT* framework, the improved artificial potential field (IAPF) is not employed as an external heuristic bias, but is embedded directly into the tree expansion mechanism of RRT*, as presented in Algorithm 1. The influence of IAPF on the key operations of RRT* can be summarized as follows:

Sampling. The sampling process remains probabilistically complete and is not directly biased toward the minima of the potential field. Instead, a target-biased sampling strategy is adopted to improve convergence efficiency. Therefore, the IAPF does not replace stochastic sampling, but indirectly facilitates convergence by shaping the effective search region.

Node Expansion. The IAPF plays a dominant role in node expansion. At each iteration, the expansion direction is explicitly guided by the IAPF force evaluated at the nearest node. By combining the potential-field gradient with the attraction toward the sampled point, the proposed method achieves a balance between global exploration and local guidance. This represents a fundamental departure from conventional APF-guided RRT* approaches, where the potential field is typically used only as a heuristic bias.

Edge Validation. Edge validity is determined using standard geometric collision checking. The IAPF does not replace collision detection; instead, it acts as a pre-guidancemechanism that reduces the likelihood of generating infeasible or unsafe edges.

Rewiring. The rewiring process follows the standard RRT* cost-based optimization framework. In the current implementation, the IAPF is not explicitly re-evaluated during rewiring. Its influence is implicitly reflected in the spatial distribution of nodes, which has already been shaped by the IAPF-guided expansion process. This preserves the asymptotic optimality of RRT* while improving convergence efficiency.

3.7. Theoretical Discussion

The proposed IAPF-RRT* framework introduces potential-field-based guidance into the sampling and node expansion processes of RRT*, which may influence its theoretical properties. In this subsection, a qualitative analysis is provided to clarify its impact on probabilistic completeness, asymptotic optimality, and computational complexity.

Probabilistic completeness. The proposed method preserves global random sampling with a nonzero probability. Specifically, the target-biased sampling probability p satisfies $0 < p < 1$, ensuring that uniform random sampling over the free space is retained with probability $1 - p$. Therefore, the probability of eventually sampling any region in the feasible space remains nonzero. Under this condition, the proposed method inherits the probabilistic completeness property of RRT-based planners.

Asymptotic optimality. The asymptotic optimality of RRT* relies on specific conditions, including uniform sampling over the free space and the use of a shrinking neighborhood radius for rewiring. In the proposed method, the introduction of IAPF guidance modifies the effective sampling distribution and node expansion direction. As a result, the strict theoretical assumptions required for asymptotic optimality may no longer be fully satisfied. Since uniform random sampling is still preserved with nonzero probability, the method maintains a certain level of exploration capability. From a practical perspective, the IAPF guidance improves convergence speed and solution quality in finite-time scenarios, even though strict asymptotic optimality is not formally guaranteed. Therefore, the proposed method can be interpreted as a guided variant of RRT*, where optimality is approached empirically rather than theoretically ensured.

Algorithm 1 IAPF-RRT* Path-Planning Algorithm

Input: start point q_{init}, goal point q_{goal}, obstacle set X_{obs}, maximum iterations N, step size Δd, base sampling bias p_0, sampling bias range $p \in [p_{min},\ p_{max}]$, APF parameters k_{att}, k_{rep}, ρ_o, n, weighting factors λ_1, λ_2, neighborhood radius upper bound η, rewiring constant γ_{RRT^*}, local minimum threshold ε
Output: final path P

$V \leftarrow \{q_{init}\}$; $E \leftarrow \varnothing$; $G \leftarrow (V, E)$
for iter = 1 to N **do**
  Generate a random number ξ ~ U(0, 1);
  $p_{iter} \leftarrow$ UpdateBias(p_0, X_{obs}, iter)
  if $\xi \le p_{iter}$ **then**
  $q_{rand} \leftarrow$ SampleGoalRegion(q_{goal})
  else
  $q_{rand} \leftarrow$ SampleFreeSpace()
  end if
  $q_{nearest} \leftarrow Nearest(V, q_{rand})$;
  $F_{att} \leftarrow EvaluateAttractiveForce\ (q_{nearest}, q_{goal})$; $\longrightarrow$ Equation (3)
  $F_{rep} \leftarrow EvaluateCorrectedRepulsiveForce(q_{nearest}, X_{obs}, \rho_o, n)$; $\longrightarrow$ Equation (11)
  if dynamic obstacle exists **then**
    $F_{rep} \leftarrow EvaluateVelocityAwareRepulsiveForce(q_{nearest}, X_{obs})$; $\longrightarrow$ Equation (26)
  end if
  if $\left\|F_{att} + F_{rep}\right\| < \varepsilon$ **then**
    $q_{sub} \leftarrow GenerateVirtualSubGoal(q_{nearest}, q_{goal}, X_{obs})$; $\longrightarrow$ Equations (18)–(23)
    $F_{att} \leftarrow EvaluateAttractiveForce(q_{nearest}, q_{sub})$;
  end if
  $F_{total} \leftarrow \lambda_1(F_{att} + F_{rep}) + \lambda_2 F_r$; $\longrightarrow$ Equations (29)–(32)
  $q_{new} \leftarrow$ Steer($q_{nearest}$, F_{total}, Δd); $\longrightarrow$ Equation (33)
  if $CollisionFree(q_{nearest},\ q_{new})$ **then**
    $R_{near} \leftarrow min[\gamma_{\mathrm{RRT}^*}\ (\log(\mathrm{card}(V))/\mathrm{card}(V))^{1/d}, \eta]$;
    $Q_{near} \leftarrow Near(V, q_{new}, R_{near})$;
    $q_{parent} \leftarrow ChooseBestParent(Q_{near}, q_{new})$;
    $V \leftarrow V \cup \{q_{new}\}$;
    $E \leftarrow E \cup \{(q_{parent}\ , q_{new})\}$;
    $Rewire(G, q_{new}, Q_{near})$;
  end if
end for
$P \leftarrow ExtractPath(G, q_{goal})$;
$P \leftarrow LoopPruning(P)$;
$P \leftarrow NURBSSmoothing(P)$;
Return P

Computational complexity. The computational complexity of the proposed method remains comparable to that of RRT*, which is typically expressed as $O(n\log n)$, where n denotes the number of nodes in the tree. The additional computational cost arises from the evaluation of the artificial potential field during node expansion. Since the potential field computation is local and depends only on nearby obstacles, its cost can be regarded as $O(1)$ per expansion under typical assumptions of bounded obstacle density. The overall complexity remains $O(n\log n)$, with a moderate constant-factor increase due to guidance evaluation.

The proposed IAPF-RRT* framework preserves probabilistic completeness and maintains comparable computational complexity to RRT*. While the strict theoretical guarantees of asymptotic optimality may be affected by the guided sampling mechanism, the method achieves improved convergence efficiency and trajectory quality in practical finite-time applications. This reflects a trade-off between strict theoretical optimality and practical solution quality.

4. Results and Discussion: Simulation and Field Validation

This section presents the simulation and field experimental results of the proposed IAPF-RRT* method. The performance of the algorithm is evaluated under various representative scenarios, and the results are further discussed in comparison with existing methods to highlight its effectiveness, robustness, and practical applicability.

4.1. Parameter Settings

All simulations were conducted in MATLAB R2023b on a 64-bit Windows 10 platform equipped with an Intel(R) Core (TM) i5-8300H CPU, using a single-threaded implementation. The main parameters are summarized in Table 2.

Table 2. Experimental parameter setting.

Parameter	Symbol	Value
Attractive potential gain coefficient	k_{att}	0.6
Repulsive potential gain coefficient	k_{rep}	18
Maximum obstacle influence distance/m	ρ_o	20
Repulsion correction factor	n	1.5
Step size/m	Δd	1.8
Base sampling bias	p_0	0.025
Sampling bias probability range	p	[0.025, 0.4]
Maximum number of iterations	N	10,000

The parameter values were selected based on the physical constraints of the UUV platform and commonly adopted settings in related studies, and were further fine-tuned to balance convergence efficiency, obstacle avoidance, and path smoothness. To ensure a fair comparison, all algorithms were evaluated under identical experimental conditions, including the same environment models, collision checking procedures, maximum iteration limits, and termination criteria. Key parameters were consistently applied across all methods where applicable. Random seeds were fixed to ensure reproducibility. The reported planning time includes node expansion, collision checking, and rewiring. Unless otherwise specified, all baseline methods were implemented following their original formulations without modification.

The reported smoothness values are computed based on the postprocessed trajectories. Specifically, a NURBS-based path refinement method is applied to the raw planner output to improve trajectory continuity and curvature smoothness. The postprocessing step is consistently applied to all compared methods to ensure a fair evaluation. The reported planning time includes both the planning process and the postprocessing stage. For completeness, it should be noted that the relative performance trends remain consistent between raw and postprocessed trajectories, indicating that the improvements mainly stem from the proposed planning strategy rather than the smoothing procedure.

To ensure clarity and reproducibility, the evaluation metrics used in this study are formally defined as follows.

1. Success Rate. The success rate is defined as the ratio of successful runs to the total number of trials:
$$SR = \frac{N_{\text{success}}}{N_{total}} \times 100\% \tag{37}$$
where N_{success} is the number of successful path planning trials, and N_{total} is the total number of runs.

2. Planning Time. The planning time is defined as the total computation time required to generate a feasible path, including node expansion, collision checking, rewiring, and postprocessing:
$$T = t_{planning} + t_{post} \tag{38}$$
where $t_{planning}$ denotes the path planning time, and t_{post} denotes the postprocessing time.

3. Smoothness. The Smoothness is calculated as the average angular variation between consecutive path segments, defined as
$$S = \frac{1}{N-2} \sum_{i=2}^{N-1} \arccos\left(\frac{(p_i - p_{i-1}) \cdot (p_{i+1} - p_i)}{\|p_i - p_{i-1}\| \cdot \|p_{i+1} - p_i\|} \right) \tag{39}$$
where p_i denotes the path waypoint.

4. Smoothness Normalization. To enable fair comparison across different scenarios, the smoothness values are normalized with respect to the maximum observed curvature variation:
$$S_{norm} = \frac{S}{S_{\max}} \tag{40}$$

5. Number of sharp turning points. A sharp turning point is defined as a waypoint where the turning angle exceeds a predefined threshold θ_{th}. The number of sharp turns is computed as
$$N_{turn} = \sum_{i=2}^{N-1} II(\theta_i > \theta_{th}) \tag{41}$$
where $II(\cdot)$ is the indicator function, and θ_{th} is set to 30° as the turning angle threshold.

6. Energy consumption. The energy consumption is estimated based on the trajectory length and motion smoothness:
$$E = \alpha L + \beta \sum_{i=2}^{N-1} |\theta_i| \tag{42}$$
where L is the path length, θ_i is the turning angle, and α, β are weighting coefficients reflecting propulsion and maneuvering energy costs.

4.2. Performance Analysis of the Proposed IAPF Strategy

This experiment aims to isolate and validate the effectiveness of the proposed IAPF enhancements by addressing three critical limitations of conventional APF methods, namely target non-reachability, susceptibility to local minima, and inadequate performance in dynamic obstacle environments. Comparative simulations are conducted between APF and IAPF under representative challenging scenarios to quantitatively assess improvements in robustness and local adaptability. The simulations were conducted using a grid-based map as the virtual environment. Obstacle regions were expanded through grid inflation to emulate the safety distance constraints required for UUV operation in real navigation scenarios, thereby ensuring both the feasibility and safety of the planned paths.

In this study, dynamic obstacles are modeled using a constant-velocity motion model, where each obstacle moves with a predefined velocity vector within the workspace. The motion direction and speed are assumed to be piecewise constant over short time intervals, which is consistent with common assumptions in marine environments. To account for environmental uncertainty and dynamic interactions, a reactive re-planning strategy is adopted. The planner operates in a receding-horizon manner, where the path is updated at a fixed frequency of 2 Hz. At each planning cycle, the latest obstacle states are incorporated, and the path is re-generated based on the current environment. The proposed IAPF-RRT* framework incorporates obstacle motion implicitly through velocity-aware potential field modeling. Specifically, the repulsive potential is adjusted according to the relative velocity between the UUV and dynamic obstacles, enabling adaptive avoidance behavior during node expansion. It should be noted that time-parameterized planning is not explicitly considered in this work. Instead, the focus is on efficient spatial re-planning under dynamic conditions, which is more suitable for real-time UUV applications.

Figures 10–13 depict the path-planning outcomes in diverse environmental scenarios, showing the comparative performance of the APF and IAPF algorithms. Figure 10a illustrates a scenario in which the APF algorithm faces a target unreachability problem due to an obstacle obstructing the direct path to the target point. In contrast, Figure 10b demonstrates the successful resolution of this problem using the IAPF algorithm. By dynamically adjusting the repulsive force intensity, the repulsive effects generated by obstacles and the attractive force toward the target are synchronously attenuated to zero as the UUV approaches the goal, thereby ensuring that the UUV can successfully reach the target point. Three representative local minimum trap environments were first constructed, namely single obstacle, symmetric obstacles, and U-shaped obstacles, as illustrated in Figure 11. In Figure 11a–c, the APF algorithm traps a local minimum, causing the path-planning process to abruptly halt. In Figure 11d–f, the IAPF algorithm achieves effective path planning in scenarios involving single obstacles, symmetric obstacles, and U-shaped obstacles, successfully resolving the issue of the UUV being trapped in local minima. Figure 12a shows a dynamic obstacle avoidance scenario, which is susceptible to collisions when using the APF algorithm. Figure 12b illustrates efficient and safe path planning performance achieved by the IAPF algorithm. By computing the relative velocity between the UUV and dynamic obstacles, the IAPF triggers an adaptive obstacle-avoidance strategy, thereby enhancing the adaptability of the UUV in complex dynamic environments. The comparative path planning experiment in a complex environment is shown in Figure 13. As shown in Figure 13a, the conventional APF method fails to effectively avoid dynamic obstacles during path planning. Moreover, due to the repulsive force generated by obstacles near the target exceeding the attractive force toward the goal, the UUV exhibits oscillatory behavior in the vicinity of the target, resulting in a target non-reachability problem. As illustrated in Figure 13b, the IAPF algorithm enables adaptive avoidance of dynamic obstacles and successfully guides the UUV to reach the target point.

Each algorithm was independently executed 30 times in a complex environment to evaluate its stability and robustness. The results are reported as mean $\pm$ standard deviation. Key performance metrics, including path length, planning time, number of path points, number of sharp turning points, and navigation energy consumption, were recorded. The statistical results are presented in Table 3.

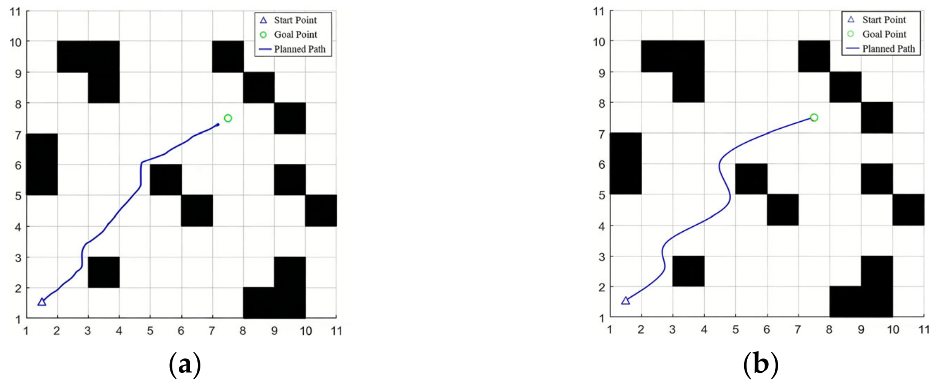

Figure 10. Comparison of the problem of unreachable goals: (**a**) APF; (**b**) IAPF.

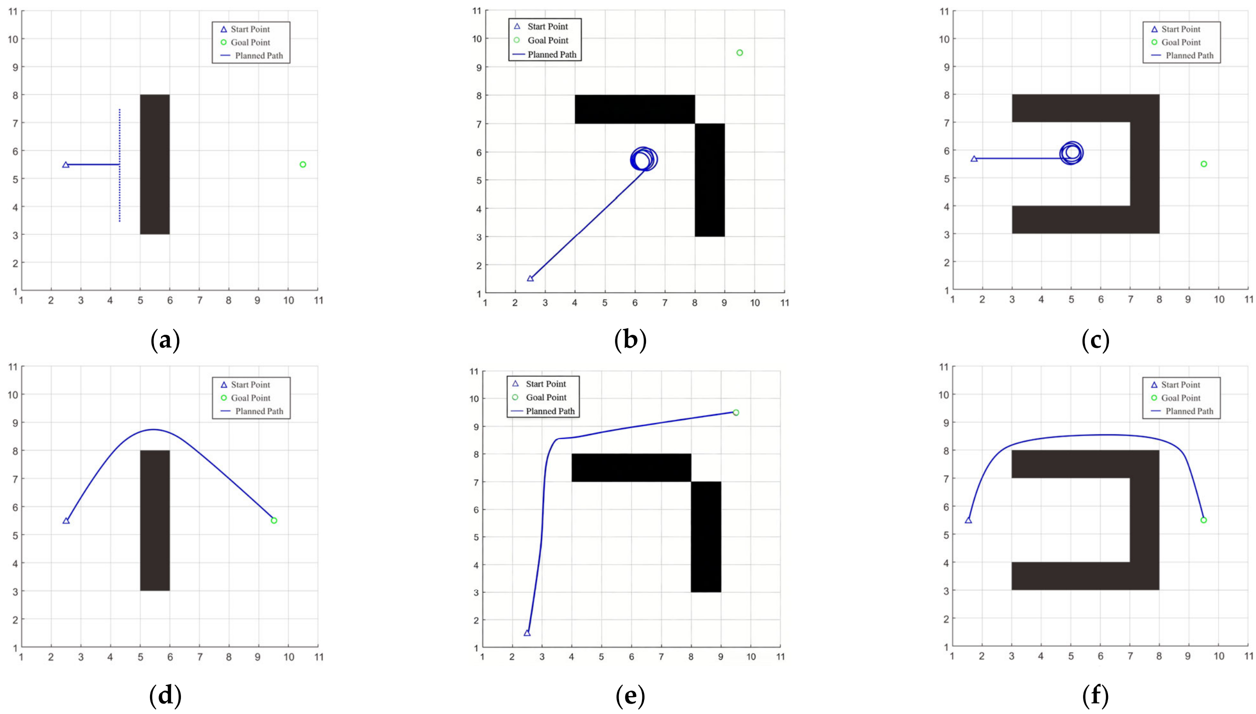

Figure 11. Comparison of the local minimum problem: (**a**) single obstacle scenario (APF); (**b**) symmetric obstacles (APF); (**c**) U-shaped obstacles (APF); (**d**) single obstacle scenario (IAPF); (**e**) symmetric obstacles (IAPF); (**f**) U-shaped obstacles (IAPF).

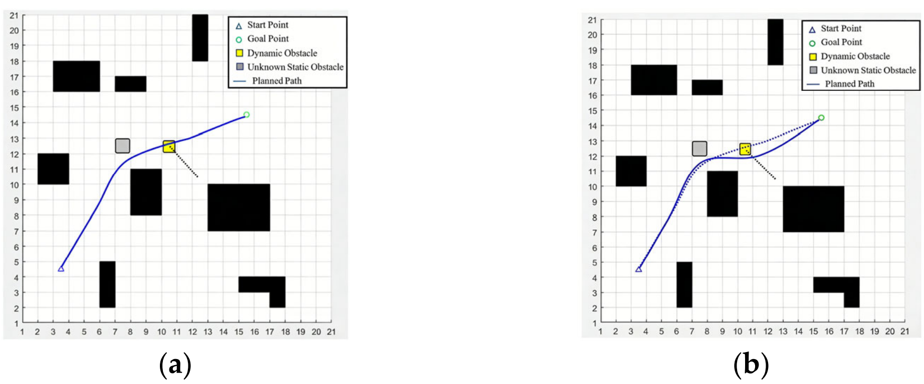

Figure 12. Comparison of dynamic obstacle avoidance: (**a**) APF; (**b**) IAPF.

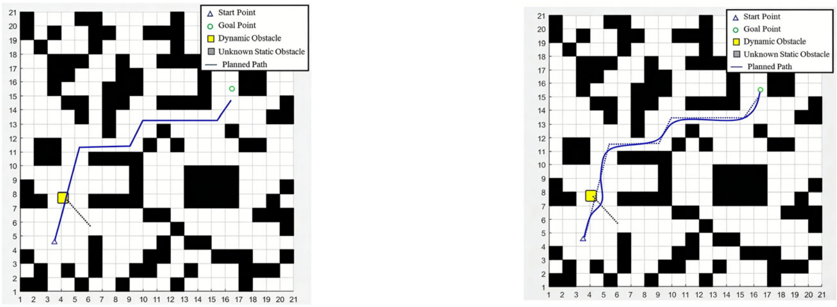

(**a**) (**b**)

Figure 13. Comparative experiment between APF and IAPF in complex environment: (**a**) APF; (**b**) IAPF.

Table 3. Comparison of experimental data.

Algorithm	Path Length (m)	Planning Time (s)	Number of Path Points	Number of Sharp Turning Points	Energy Consumption
APF	86.9 ± 3.8	5.8 ± 0.6	17 ± 3	4 ± 1	83.5 ± 5.2
IAPF	73.9 ± 2.9	2.4 ± 0.3	12 ± 2	0	52.8 ± 3.4

The quantitative results in Table 3 demonstrate that the proposed IAPF algorithm consistently outperforms the conventional APF method. All experiments were repeated 30 times under identical conditions, and the results are reported as mean ± standard deviation. It can be observed that the IAPF algorithm achieves a shorter average path length (73.9 ± 2.9 m) compared with APF (86.9 ± 3.8 m), corresponding to a reduction of approximately 15.0%. Meanwhile, the planning time is significantly reduced from 5.8 ± 0.6 s to 2.4 ± 0.3 s, indicating an improvement in computational efficiency of approximately 58.6%. In addition, the average number of path points is reduced from 17 ± 3 to 12 ± 2, reflecting a more concise trajectory representation. Notably, sharp turning points are completely eliminated (0 ± 0), demonstrating that the proposed method effectively suppresses abrupt directional changes and improves trajectory smoothness. The energy consumption is reduced from 83.5 ± 5.2 to 52.8 ± 3.4, corresponding to a reduction of approximately 36.8%, which indicates improved energy efficiency and operational endurance. These results demonstrate that the IAPF algorithm enhances convergence efficiency, path smoothness, and energy efficiency, making it more suitable for dynamic path planning in complex environments.

4.3. Simulation-Based Evaluation of the IAPF-RRT Algorithm*

This subsection evaluates the performance of the proposed IAPF-RRT* algorithm as a global path-planning framework. A series of simulation scenarios with increasing complexity was designed to assess the method in terms of planning efficiency, path quality, and robustness. Considering that UUVs primarily operate in two-dimensional planes while occasionally performing three-dimensional maneuvers, both 2D and 3D environments were constructed. To ensure a comprehensive and fair evaluation, six representative state-of-the-art (SOTA) baseline algorithms were selected, including classical sampling-based methods (RRT [23], RRT* [26]), structure-enhanced variants (Bi-RRT* [31], Informed-RRT* [28]), and guided sampling approaches (APF-RRT* [38], Bi-APF-RRT* [40]). All baseline methods were implemented according to their standard formulations. For hybrid approaches, the potential field was incorporated as a heuristic guidance term during node expansion, following common practices in the literature. All methods were evaluated under identical experimental conditions, including the same environment settings, collision checking procedures, maximum iteration limits, and termination criteria, without additional modifications or parameter tuning. This setup ensures a rigorous and unbiased comparison with existing SOTA algorithms.

4.3.1. 2D Simulation Scenarios

The two-dimensional simulation environments were designed to reflect representative navigation conditions encountered by UUVs in nearshore regions. Four typical scenarios were constructed, including sparse obstacle, dense obstacle, narrow passage, and complex mixed environments, as shown in Figure 14. The workspace was defined as a 100 m × 100 m planar area, where dark regions denote obstacles and blank regions represent free space. The UUV's start and target points were set to (0, 0) and (100, 100), respectively. To ensure statistical reliability, each algorithm was independently executed 30 times under identical experimental conditions.

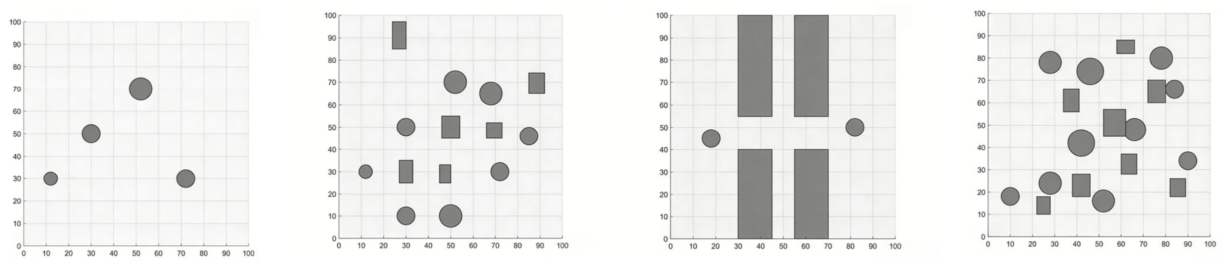

(**a**) (**b**) (**c**) (**d**)

Figure 14. Simulation environments: (**a**) sparse obstacle environment; (**b**) dense obstacle environment; (**c**) narrow passage environment; (**d**) complex mixed environment. The grey shading shapes represent obstacles.

1. Sparse Obstacle Environment

In this scenario, only a limited number of obstacles were distributed within the workspace, resulting in relatively open navigation conditions. This setting is primarily used to evaluate the baseline performance of each algorithm in terms of convergence efficiency and path feasibility. The simulation results are shown in Figure 15, and the red line represents the path track of the UUV planned by the algorithms.

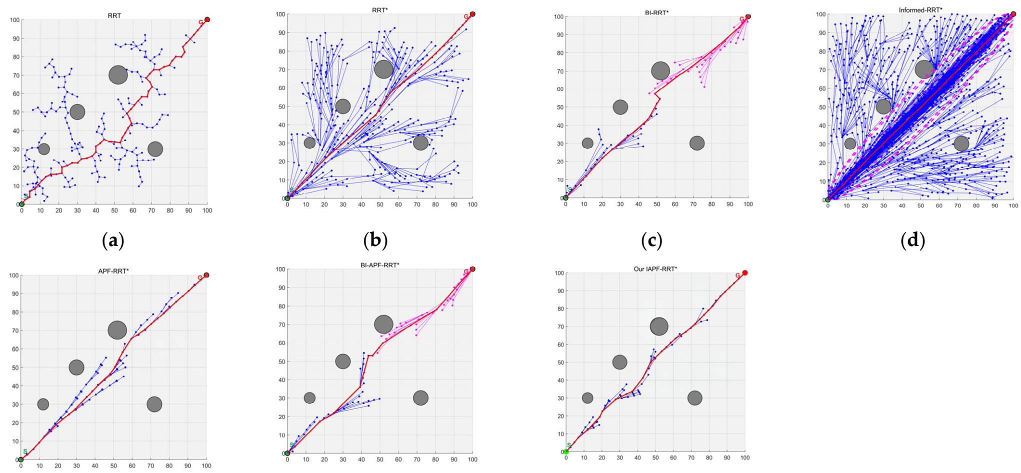

(**a**) (**b**) (**c**) (**d**)

(**e**) (**f**) (**g**)

Figure 15. Path planning results in sparse obstacle environment: (**a**) RRT; (**b**) RRT*; (**c**) Bi-RRT*; (**d**) Informed-RRT*; (**e**) APF-RRT*; (**f**) Bi-APF-RRT*; (**g**) our IAPF-RRT*.In each subfigure, the red line denotes the final path generated by the corresponding algorithm, the green "S" marks the starting position, the red "G" indicates the goal location, and the grey shading shapes represent obstacles.

The performance was evaluated using multiple metrics, including path length, planning time, node count, trajectory smoothness, success rate, and the average number of iterations. The results for different scenarios are summarized in Table 4, providing a comprehensive comparison under varying environmental conditions. All results are reported as mean ± standard deviation over multiple independent runs. The mean reflects the overall performance of each algorithm, while the standard deviation indicates its stability and robustness. Lower mean values and smaller standard deviations correspond to better performance and higher consistency in path planning. A comprehensive summary of the corresponding performance indicators is provided in the following subsection.

Table 4. Performance comparison under different scenarios (mean ± std over 30 runs).

Scenario	Algorithm	Path Length (m)	Planning Time (s)	Number of Random-Tree Nodes	Smoothness [1]	Success Rate [1] %	Average Iterations
Sparse obstacle environment	RRT	166.75 ± 4.86	0.79 ± 0.11	230 ± 28	3.5 ± 0.29	100.00	230 ± 32
	RRT*	141.94 ± 2.12	6.61 ± 0.74	354 ± 33	2.6 ± 0.18	100.00	358 ± 45
	Bi-RRT*	142.51 ± 1.68	0.75 ± 0.10	76 ± 9	2.4 ± 0.15	100.00	37 ± 6
	Informed-RRT*	141.45 ± 1.94	12.84 ± 1.63	1950 ± 150	2.8 ± 0.21	100.00	1982 ± 24
	APF-RRT*	142.40 ± 1.27	0.78 ± 0.09	102 ± 11	1.9 ± 0.10	100.00	100 ± 14
	Bi-APF-RRT*	143.39 ± 1.11	0.67 ± 0.08	70 ± 8	2.1 ± 0.12	100.00	34 ± 5
	Our IAPF-RRT*	143.14 ± 0.88	0.89 ± 0.07	95 ± 9	1.8 ± 0.07	100.00	126 ± 15
Dense obstacle environment	RRT	160.58 ± 5.42	0.85 ± 0.13	220 ± 31	4.2 ± 0.36	93.33	243 ± 36
	RRT*	149.51 ± 3.06	6.31 ± 0.68	250 ± 27	3.2 ± 0.24	96.67	302 ± 38
	Bi-RRT*	142.95 ± 2.10	2.25 ± 0.31	119 ± 15	2.9 ± 0.19	100.00	85 ± 11
	Informed-RRT*	142.83 ± 2.45	14.51 ± 1.92	1720 ± 214	3.5 ± 0.28	93.33	1975 ± 31
	APF-RRT*	142.50 ± 1.56	1.02 ± 0.11	72 ± 11	2.4 ± 0.15	100.00	124 ± 17
	Bi-APF-RRT*	141.00 ± 1.21	1.10 ± 0.13	73 ± 8	2.5 ± 0.16	100.00	36 ± 6
	Our IAPF-RRT*	142.78 ± 0.97	0.98 ± 0.09	96 ± 10	2.2 ± 0.09	100.00	116 ± 14
Narrow passage environment	RRT	219.12 ± 8.95	1.16 ± 0.18	350 ± 44	5.5 ± 0.48	80.00	561 ± 72
	RRT*	149.14 ± 3.42	2.04 ± 0.27	193 ± 24	3.8 ± 0.26	90.00	248 ± 34
	Bi-RRT*	175.47 ± 6.38	1.82 ± 0.24	161 ± 22	3.5 ± 0.24	96.67	144 ± 21
	Informed-RRT*	147.82 ± 3.18	9.93 ± 1.41	1430 ± 188	3.6 ± 0.27	86.67	1988 ± 22
	APF-RRT*	149.67 ± 2.76	1.27 ± 0.16	182 ± 21	2.8 ± 0.18	93.33	232 ± 30
	Bi-APF-RRT*	147.05 ± 1.84	0.74 ± 0.09	88 ± 11	3.0 ± 0.22	96.67	60 ± 9
	Our IAPF-RRT*	146.90 ± 1.12	1.01 ± 0.11	130 ± 14	2.5 ± 0.11	96.67	198 ± 24
Complex mixed environment	RRT	159.86 ± 6.11	1.43 ± 0.19	388 ± 46	4.8 ± 0.41	86.67	515 ± 68
	RRT*	153.53 ± 4.08	10.78 ± 1.27	302 ± 35	3.5 ± 0.27	93.33	461 ± 55
	Bi-RRT*	146.60 ± 2.44	1.62 ± 0.20	92 ± 12	3.1 ± 0.21	96.67	66 ± 10
	Informed-RRT*	143.21 ± 2.87	13.88 ± 1.75	1647 ± 205	3.3 ± 0.26	90.00	1986 ± 27
	APF-RRT*	148.79 ± 2.96	2.52 ± 0.31	155 ± 18	2.4 ± 0.16	93.33	216 ± 28
	Bi-APF-RRT*	142.56 ± 1.63	1.27 ± 0.14	78 ± 9	2.6 ± 0.18	96.67	48 ± 7
	Our IAPF-RRT*	147.88 ± 1.42	1.35 ± 0.12	135 ± 15	2.3 ± 0.09	100.00	237 ± 26

[1] Success rate was calculated from 30 trials.

Figure 15 presents a qualitative comparison between the proposed method and several representative state-of-the-art (SOTA) algorithms. The RRT algorithm generates highly random trajectories with numerous inflection points, resulting in long and non-smooth paths. As shown in Figure 15b, RRT* improves path optimality but still produces redundant branches. The Bi-RRT* algorithm in Figure 15c enhances convergence speed and reduces node redundancy, but the generated paths still lack smoothness. In Figure 15d, Informed-RRT* improves search efficiency by constraining the sampling region, but redundant expansions around obstacles remain. The APF-RRT* algorithm in Figure 15e enhances obstacle avoidance, while Bi-APF-RRT* in Figure 15f further reduces redundant branches and improves efficiency, although minor irregularities persist. In contrast, the proposed IAPF-RRT* algorithm in Figure 15g generates smoother and more stable paths with significantly fewer branches, demonstrating stronger directionality and robustness. To ensure statistical reliability, all experiments were independently repeated 30 times under identical conditions, and the results are reported as mean ± standard deviation in Table 4. Under the sparse obstacle environment, the proposed IAPF-RRT* achieves the lowest average smoothness (1.8 ± 0.07), which is reduced by approximately 14.3% and 5.3% compared with Bi-APF-RRT* (2.1 ± 0.12) and APF-RRT* (1.9 ± 0.10), respectively. In terms of computational efficiency, the proposed method significantly reduces the planning time compared with RRT* (6.61 ± 0.74 s) and Informed-RRT* (12.84 ± 1.63 s), while also effectively suppressing redundant node expansion. Although the path length is slightly higher than that of Bi-APF-RRT* (approximately 0.2% difference on average), the proposed method achieves a better balance among path smoothness, computational efficiency, and stability.

2. Dense Obstacle Environment

To evaluate the performance of the proposed algorithm in cluttered environments, multiple obstacles were randomly distributed to form a densely populated workspace. In this scenario, the straight-line path between the start and goal positions is significantly obstructed, requiring efficient global exploration and effective obstacle avoidance. The trajectories planned by the seven algorithms are shown in Figure 16.

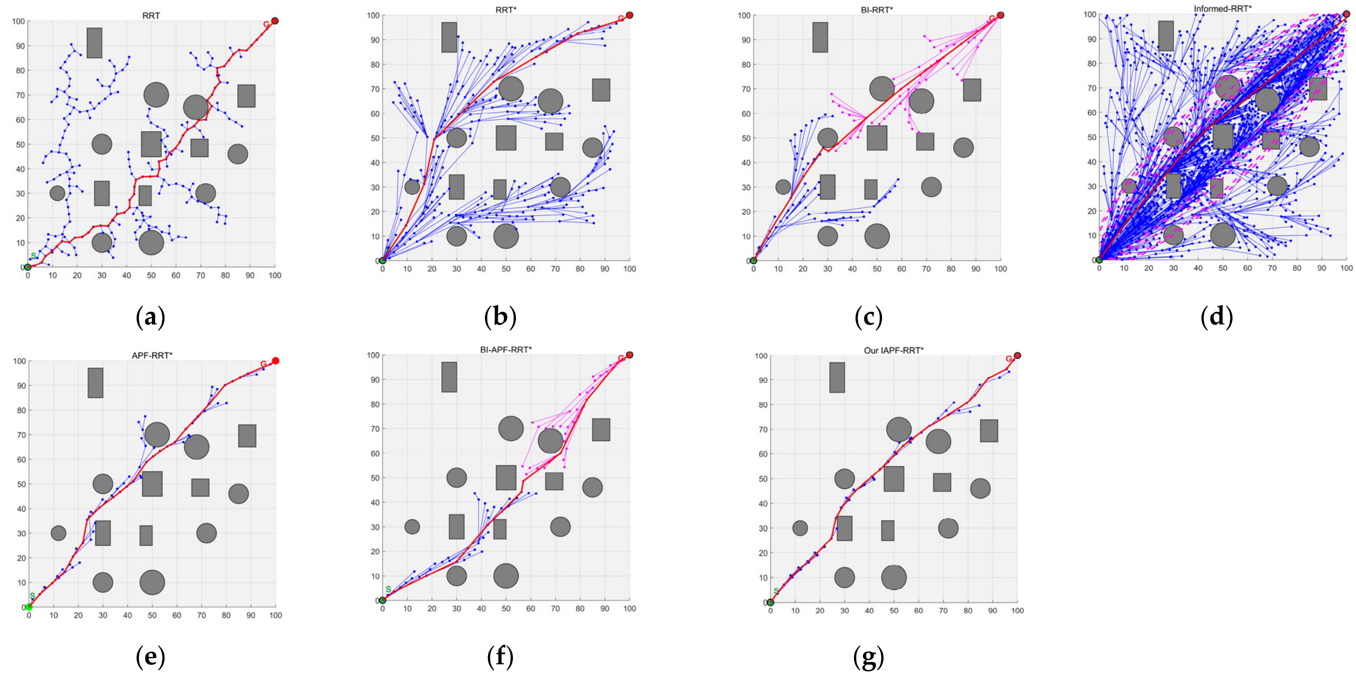

Figure 16. Path planning comparison in dense obstacle environment: (**a**) RRT; (**b**) RRT*; (**c**) Bi-RRT*; (**d**) Informed-RRT*; (**e**) APF-RRT*; (**f**) Bi-APF-RRT*; (**g**) our IAPF-RRT*. In each subfigure, the red line denotes the final path generated by the corresponding algorithm, the green "S" marks the starting position, the red "G" indicates the goal location, and the grey shading shapes represent obstacles.

As illustrated in Figure 16, in the dense obstacle environment, the RRT and RRT* algorithms generate a large number of sampling nodes distributed across the entire workspace in order to obtain a feasible path, resulting in significant redundancy and reduced search efficiency. In contrast, the Bi-RRT* and Informed-RRT* algorithms improve convergence speed by adopting bidirectional expansion and constrained sampling strategies, respectively. However, although Informed-RRT* effectively limits the sampling region, it still produces excessive redundant nodes around obstacles due to the lack of obstacle-aware guidance. The APF-RRT* algorithm introduces artificial potential field guidance, which enhances obstacle avoidance capability and improves the rationality of the planned path. Nevertheless, local oscillations and redundant branches can still be observed in cluttered regions. Compared with APF-RRT*, the Bi-APF-RRT* algorithm further accelerates path generation by combining bidirectional expansion with potential field guidance, leading to fewer sampling nodes and a more efficient search process. As shown in Figure 16g, the proposed IAPF-RRT* algorithm significantly reduces the number of redundant nodes while maintaining strong goal-directed exploration. By integrating an improved goal-bias strategy with enhanced potential field guidance, the algorithm achieves faster convergence and generates a smoother and more natural path. In addition, the resulting trajectory exhibits better adaptability to densely distributed obstacles, making it more suitable for practical path planning tasks in complex environments.

The quantitative results in Table 4 demonstrate that the proposed method consistently outperforms representative state-of-the-art (SOTA) algorithms in dense environments. To ensure statistical reliability, all experiments were independently repeated 30 times under identical conditions, and the results are reported as mean ± standard deviation. It can be observed that the proposed IAPF-RRT* algorithm achieves significantly improved computational efficiency, with a lower average planning time (0.98 ± 0.09 s) compared with RRT* (6.31 ± 0.68 s) and Informed-RRT* (14.51 ± 1.92 s). Meanwhile, the average number of nodes is substantially reduced (96 ± 10), indicating effective suppression of redundant exploration compared with RRT*-based methods. In addition, the proposed method achieves improved trajectory smoothness (2.2 ± 0.09) compared with APF-based methods, such as APF-RRT* (2.4 ± 0.15) and Bi-APF-RRT* (2.5 ± 0.16), while maintaining a 100.00% success rate. The proposed method demonstrates more efficient, stable, and consistent path planning performance in dense and cluttered environments.

3. Narrow Passage Environment

A narrow passage scenario was constructed to assess the sampling efficiency and exploration capability of different algorithms in constrained spaces. In this environment, the feasible path from the start to the goal is restricted to one or more narrow corridors, which are difficult to discover through purely random sampling. The simulation path diagram of each algorithm is shown in Figure 17.

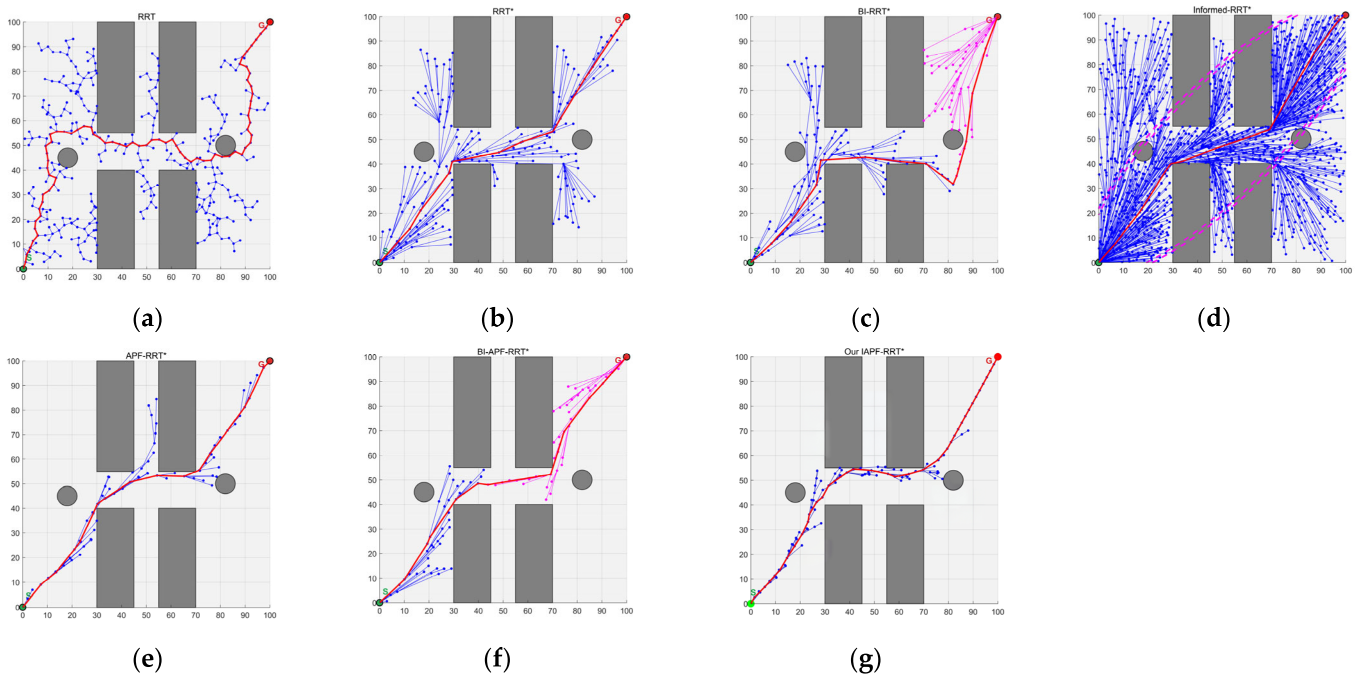

Figure 17. Path planning results in narrow passage environment: (**a**) RRT; (**b**) RRT*; (**c**) Bi-RRT*; (**d**) Informed-RRT*; (**e**) APF-RRT*; (**f**) Bi-APF-RRT*; (**g**) our IAPF-RRT*. In each subfigure, the red line denotes the final path generated by the corresponding algorithm, the green "S" marks the starting position, the red "G" indicates the goal location, and the grey shading shapes represent obstacles.

As illustrated in Figure 17, the narrow passage environment imposes strict constraints on feasible paths. The classical RRT and RRT* algorithms exhibit strong randomness and generate numerous redundant branches, making it difficult to efficiently traverse the confined region. Structure-enhanced SOTA methods, including Bi-RRT* and Informed-RRT*, improve convergence speed; however, inefficient exploration and excessive node expansion near the passage entrance still occur. The APF-RRT* and Bi-APF-RRT* algorithms enhance obstacle avoidance through potential field guidance, enabling improved navigation in narrow regions, although local deviations and redundant branches remain. In contrast, the proposed IAPF-RRT* algorithm demonstrates improved directionality and stability, effectively guiding the search through constrained passages with fewer nodes and smoother trajectories. To ensure statistical reliability, all experiments were independently repeated 30 times under identical conditions, and the results are reported as mean $\pm$ standard deviation in Table 4. Quantitatively, the proposed method achieves a lower average planning time (1.01 $\pm$ 0.1 s) compared with RRT* (2.04 $\pm$ 0.27 s) and Informed-RRT* (9.93 $\pm$ 1.41 s). The average number of nodes is also reduced (130 $\pm$ 14), indicating more efficient exploration in comparison with RRT*-based methods. In addition, improved trajectory smoothness (2.5 $\pm$ 0.11) is achieved compared with APF-based approaches, such as APF-RRT* (2.8 $\pm$ 0.18) and Bi-APF-RRT* (3.0 $\pm$ 0.22). Moreover, the proposed method maintains a high success rate (96.67%), demonstrating reliable performance in constrained environments. The results indicate that the proposed algorithm provides improved efficiency, stability, and consistency for path planning in narrow passage scenarios, as supported by statistical outcomes across multiple independent runs.

4. Complex Mixed Environment

To further approximate realistic coastal navigation conditions, a complex mixed environment was designed by combining irregular obstacle distributions with both open and cluttered regions. This scenario aims to comprehensively evaluate the robustness and adaptability of the proposed algorithm under heterogeneous spatial conditions. The path planning results of different algorithms are shown in Figure 18. Based on the above experimental results, a comprehensive comparison of the performance indicators is presented in Figure 19.

For the complex mixed environment with heterogeneous obstacle distributions, the advantages of the proposed method become more evident. As shown in Figure 18a–d, classical one-way search methods such as RRT and RRT* can eventually find feasible paths; however, they generate a large number of redundant nodes and exhibit low search efficiency. The bidirectional Bi-RRT* algorithm improves convergence speed to some extent, but the resulting paths still lack sufficient smoothness. The Informed-RRT* algorithm further accelerates convergence by constraining the sampling region; nevertheless, excessive sampling and redundant expansions around obstacles are still observed. As illustrated in Figure 18e,f, APF-RRT* and Bi-APF-RRT* enhance obstacle avoidance through potential field guidance, leading to improved path quality, although local deviations and unnecessary node expansions remain in cluttered regions. In contrast, the proposed IAPF-RRT* algorithm, as shown in Figure 18g, integrates improved goal-biased sampling with potential field guidance, enabling more directed exploration in complex environments. This results in smoother trajectories and fewer redundant nodes, thereby improving overall search efficiency. To ensure statistical reliability, all experiments were independently repeated 30 times under identical conditions, and the results are reported as mean $\pm$ standard deviation in Table 4. Quantitatively, the proposed method achieves a lower average planning time (1.35 $\pm$ 0.12 s) compared with RRT* (10.78 $\pm$ 1.27 s) and Informed-RRT* (13.88 $\pm$ 1.75 s). The average number of nodes is also reduced (135 $\pm$ 15), indicating more efficient exploration relative to RRT*-based methods. In addition, the proposed method provides improved trajectory smoothness (2.3 ± 0.09) compared with APF-based approaches, such as APF-RRT* (2.4 ± 0.16) and Bi-APF-RRT* (2.6 ± 0.18), while maintaining a high success rate (100.00%). Although the average path length is slightly higher than that of Bi-APF-RRT*, the proposed method achieves a better balance among path quality, computational efficiency, and robustness. These results demonstrate that the proposed algorithm provides improved efficiency, stability, and consistency for path planning in complex environments, as supported by statistical outcomes across multiple independent runs.

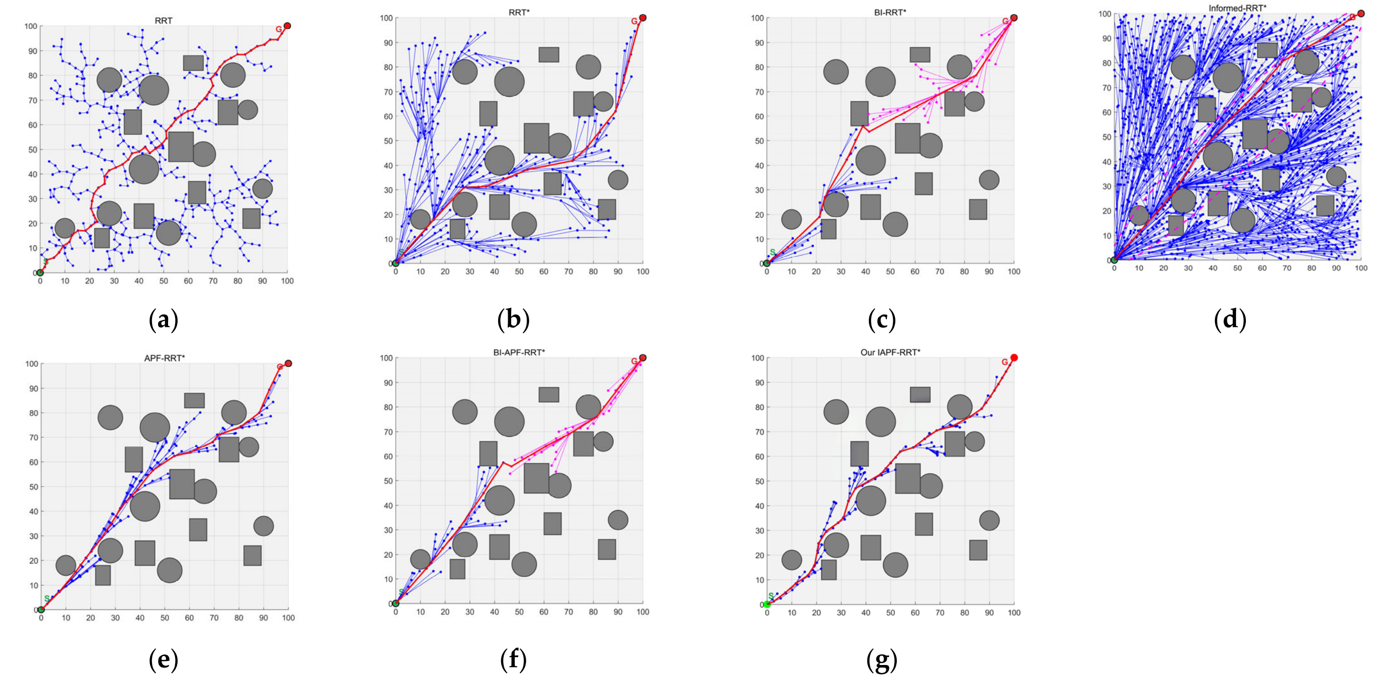

Figure 18. Path planning comparison in complex mixed environment: (**a**) RRT; (**b**) RRT*; (**c**) Bi-RRT*; (**d**) Informed-RRT*; (**e**) APF-RRT*; (**f**) Bi-APF-RRT*; (**g**) our IAPF-RRT*. In each subfigure, the red line denotes the final path generated by the corresponding algorithm, the green "S" marks the starting position, the red "G" indicates the goal location, and the grey shading shapes represent obstacles.

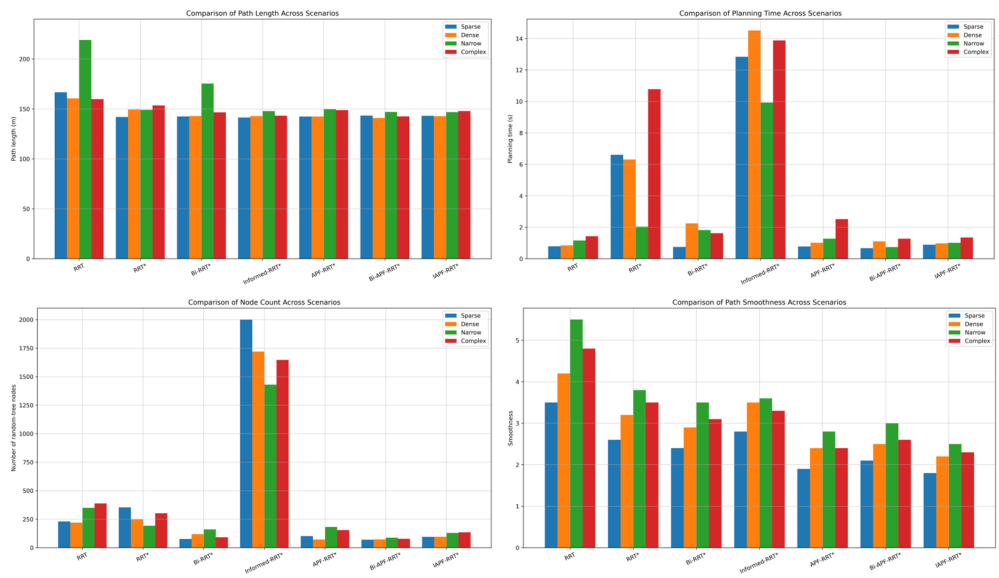

Figure 19. Comparison of algorithm evaluation indicators across four typical scenarios.

4.3.2. 3D Path Planning Simulation Experiment

To comprehensively evaluate the performance of the proposed method in realistic nearshore environments, two representative three-dimensional simulation scenarios were constructed within a cubic workspace of $[-1000, 1000]^3$. The start and goal positions of the UUV were set to $(-1000, -1000, -1000)$ and $(1000, 1000, 1000)$, respectively. Obstacles were modeled using a combination of spherical, cuboid, and cylindrical primitives to emulate natural reefs, aquaculture facilities, and supporting pile structures, thereby approximating nearshore operational conditions around Phoenix Island.

The first scenario corresponds to a narrow passage environment with aquaculture characteristics, where multiple cage-like structures and vertical piles are arranged to form a confined spatial corridor in the central region. The available free space is significantly restricted in all three dimensions, requiring the UUV to traverse a limited volumetric passage to reach the target. This scenario is designed to evaluate the capability of the algorithm in handling highly constrained environments and avoiding excessive branching during passage traversal. The second scenario represents a complex coastal environment with heterogeneous obstacle distributions. In this case, obstacles are irregularly distributed across the workspace without forming a single dominant bottleneck. Instead, multiple potential routes exist, and the UUV is required to perform continuous spatial adjustments to avoid both natural and artificial obstacles. This scenario aims to assess the robustness, adaptability, and global planning efficiency of the proposed method under realistic nearshore conditions.

By jointly considering these two scenarios, the proposed method is evaluated in terms of both constrained passage traversal and complex environment navigation, thereby providing a comprehensive validation of its effectiveness in practical coastal applications. The parameter settings in the 3D simulations are largely consistent with those in the 2D scenarios. The core algorithmic parameters (k_{att}, k_{rep}, ρ_o, n) are kept unchanged. To account for the larger search space in 3D environments, several parameters are slightly adjusted. The step size is set to $\Delta d = 2.0$ m, and the maximum number of iterations to $N = 20{,}000$. These settings balance exploration efficiency and computational cost in 3D scenarios. The experimental scenarios and the corresponding planning results are presented in Figures 20 and 21. To ensure statistical reliability, each algorithm was independently executed 30 times under identical conditions. The mean values of path length, node count, planning time, success rate, and average iterations are summarized in Table 5. To facilitate a more intuitive comparison, these results are summarized in the bar chart shown in Figure 22. The chart visually contrasts the algorithms with respect to key metrics, including path length, node count, search time, and success rate, providing an intuitive and comprehensive basis for performance evaluation and analysis.

The simulation results in Figures 20 and 21, together with the quantitative comparisons in Table 5 and the bar-chart analysis in Figure 22, demonstrate that the proposed IAPF-RRT* algorithm consistently achieves superior performance in three-dimensional environments. To ensure statistical reliability, all experiments were independently repeated 30 times under identical conditions, and the results are reported as mean $\pm$ standard deviation. In the narrow passage scenario, classical RRT and RRT* algorithms exhibit significant randomness and generate numerous redundant branches, leading to longer and less smooth paths. Although Informed-RRT* improves sampling efficiency, excessive node expansion still occurs due to insufficient obstacle guidance. In contrast, the proposed IAPF-RRT* algorithm effectively guides the search through constrained regions, achieving a shorter average path length (3567.13 ± 36.80 m) and improved trajectory smoothness (1.8 ± 0.06). Meanwhile, the average planning time (0.24 ± 0.02 s) and node count (63 ± 7) are significantly reduced compared with RRT*-based approaches, indicating effective suppression of redundant exploration. In the complex coastal environment, where obstacle distributions are more irregular and spatial constraints are stronger, the advantages of the proposed method become more pronounced. Although APF-based methods improve obstacle avoidance capability, they still suffer from local oscillations. By integrating dynamic goal bias and improved potential field guidance, the IAPF-RRT* algorithm produces smoother trajectories (1.7 $\pm$ 0.05) while maintaining a shorter path length (3600.57 $\pm$ 36.20 m). In addition, the proposed method achieves lower planning time (0.20 $\pm$ 0.02 s) and fewer nodes (43 $\pm$ 5), demonstrating more efficient exploration performance. The comparisons in Figure 22 further confirm these observations. The proposed method consistently achieves lower values in path length, planning time, node count, and smoothness across all scenarios, while maintaining a 100.00% success rate. Overall, these results indicate that the proposed IAPF-RRT* algorithm provides improved convergence efficiency, path quality, and robustness in complex three-dimensional environments, making it suitable for practical UUV path-planning tasks in nearshore and aquaculture scenarios. To further evaluate the contribution of each component in the proposed framework, an ablation study is conducted to isolate and analyze the effectiveness of individual modules.

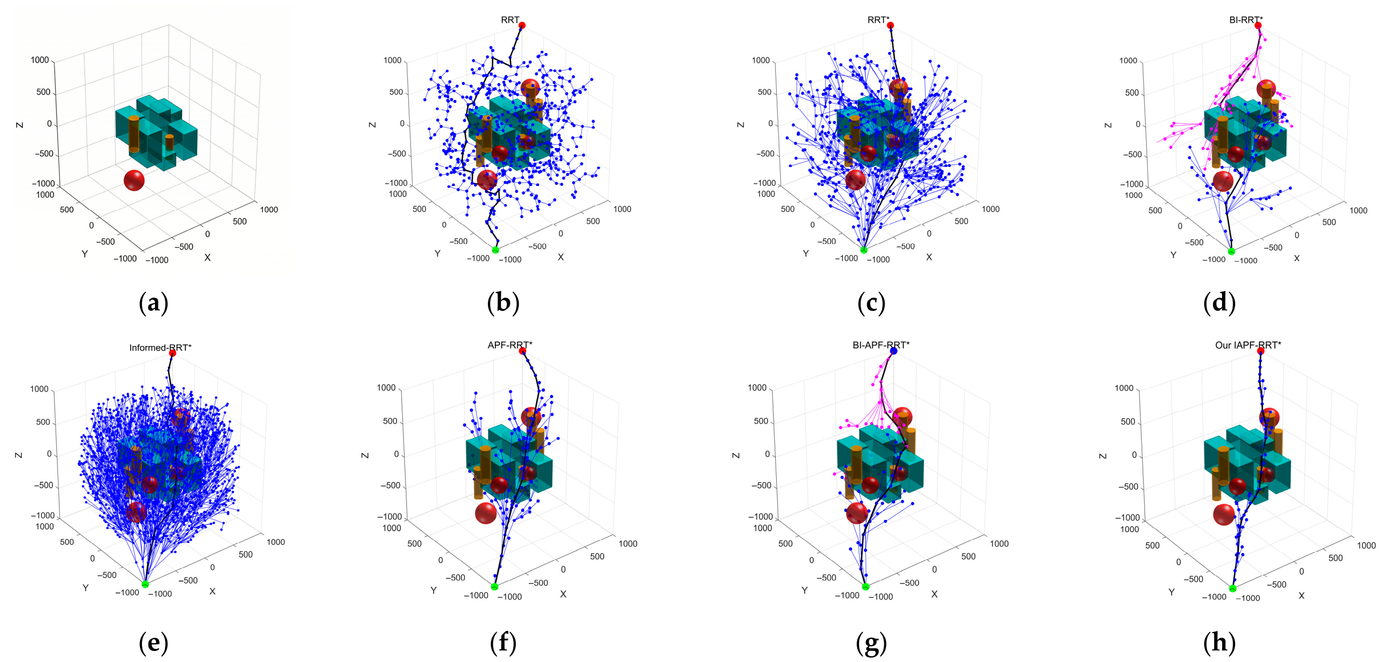

Figure 20. Path planning comparison in narrow passage environment: (**a**) narrow passage scenario; (**b**) RRT; (**c**) RRT*; (**d**) Bi-RRT*; (**e**) Informed-RRT*; (**f**) APF-RRT*; (**g**) Bi-APF-RRT*; (**h**) our IAPF-RRT*. In each subfigure, the blue line denotes the final path generated by the corresponding algorithm, and obstacles are visualized as differently colored shapes.

4.4. Ablation Study of Key Components

To further quantify the contribution of each module in the proposed framework, an ablation study was conducted by incrementally integrating key components into the baseline RRT* algorithm. This analysis aims to isolate the influence of each module on planning performance and to elucidate the underlying mechanisms responsible for the overall improvement. The ablation study was conducted in a representative complex cluttered environment with mixed static and dynamic obstacles (Scenario 4 in Section 4.3), where narrow passages, local minima, and dynamic interactions coexist. This scenario serves as a stress-test case for evaluating the effectiveness of different modules. The ablation study is conducted under the same experimental settings as the 2D simulations. Although the ablation experiments are performed in this representative scenario, the observed performance trends are consistent across the other scenarios presented in Section 4.3.

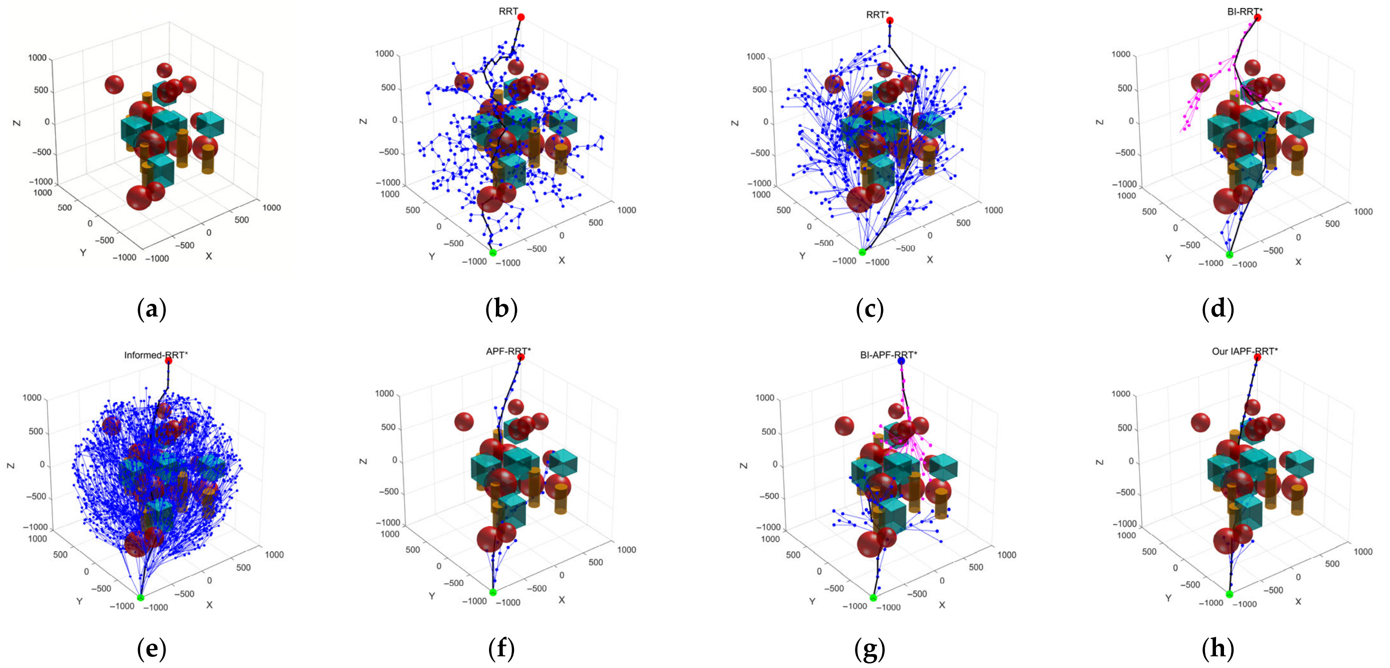

Figure 21. Path planning results in complex coastal environment: (**a**) narrow passage scenario; (**b**) RRT; (**c**) RRT*; (**d**) Bi-RRT*; (**e**) Informed-RRT*; (**f**) APF-RRT*; (**g**) Bi-APF-RRT*; (**h**) our IAPF-RRT*. In each subfigure, the blue line denotes the final path generated by the corresponding algorithm, and obstacles are visualized as differently colored shapes.

Table 5. Performance comparison of the algorithms under 3D scenarios (mean ± std over 30 runs).

Scenario	Algorithm	Path Length (m)	Planning Time (s)	Number of Random-Tree Nodes	Smoothness [1]	Success Rate [1] %	Average Iterations
narrow passage environment	RRT	4871.26 ± 126.40	1.62 ± 0.18	577 ± 61	3.8 ± 0.27	76.67	596 ± 74
	RRT*	3809.31 ± 88.70	2.68 ± 0.29	566 ± 52	3.2 ± 0.21	83.33	638 ± 66
	Bi-RRT*	3996.50 ± 95.80	0.66 ± 0.07	143 ± 16	2.6 ± 0.16	93.33	83 ± 10
	Informed-RRT*	3848.25 ± 79.60	14.33 ± 1.57	1777 ± 148	3.5 ± 0.24	76.67	1982 ± 61
	APF-RRT*	3744.32 ± 64.20	0.53 ± 0.05	134 ± 14	2.4 ± 0.13	90.00	156 ± 18
	Bi-APF-RRT*	3680.34 ± 49.50	0.31 ± 0.03	81 ± 9	2.1 ± 0.10	96.67	45 ± 6
	Our IAPF-RRT*	3567.13 ± 36.80	0.24 ± 0.02	63 ± 7	1.8 ± 0.06	100.00	104 ± 11
complex coastal environment	RRT	4737.87 ± 118.30	1.32 ± 0.15	437 ± 52	3.6 ± 0.24	83.33	469 ± 58
	RRT*	3949.36 ± 84.50	1.86 ± 0.19	428 ± 48	3.0 ± 0.19	86.67	486 ± 51
	Bi-RRT*	3986.66 ± 71.20	0.31 ± 0.03	78 ± 8	2.4 ± 0.14	96.67	59 ± 7
	Informed-RRT*	3822.87 ± 76.40	14.74 ± 1.62	1740 ± 156	3.3 ± 0.23	80.00	1987 ± 58
	APF-RRT*	3684.33 ± 48.60	0.29 ± 0.02	55 ± 6	2.2 ± 0.10	96.67	80 ± 9
	Bi-APF-RRT*	3733.81 ± 53.70	0.33 ± 0.03	108 ± 12	2.0 ± 0.09	96.67	68 ± 8
	Our IAPF-RRT*	3600.57 ± 36.20	0.20 ± 0.02	43 ± 5	1.7 ± 0.05	100.00	87 ± 9

[1] Success rate was calculated from 30 trials.

Five variants were considered: M1, baseline RRT*; M2, RRT* with IAPF guidance; M3, M2 with target-biased sampling; M4, M3 with adaptive attraction weighting; and M5, M4 with path refinement (the full proposed method). Each method was evaluated over 30 independent runs to reduce the influence of randomness. All experiments were repeated 30 times under identical conditions to account for the stochastic nature of sampling-based planning algorithms. The reported values correspond to the mean and standard deviation of each metric. The performance was assessed using the following metrics: path length (m), planning time (s), number of nodes, smoothness index, and success rate (%). The number of iterations is not explicitly reported, as the planning time and node count already reflect the computational efficiency of the proposed method. The corresponding results are presented in Table 6. In addition, to further evaluate the effectiveness of the velocity-aware obstacle avoidance strategy, an ablation study was conducted under dynamic obstacle scenarios, as summarized in Table 7.

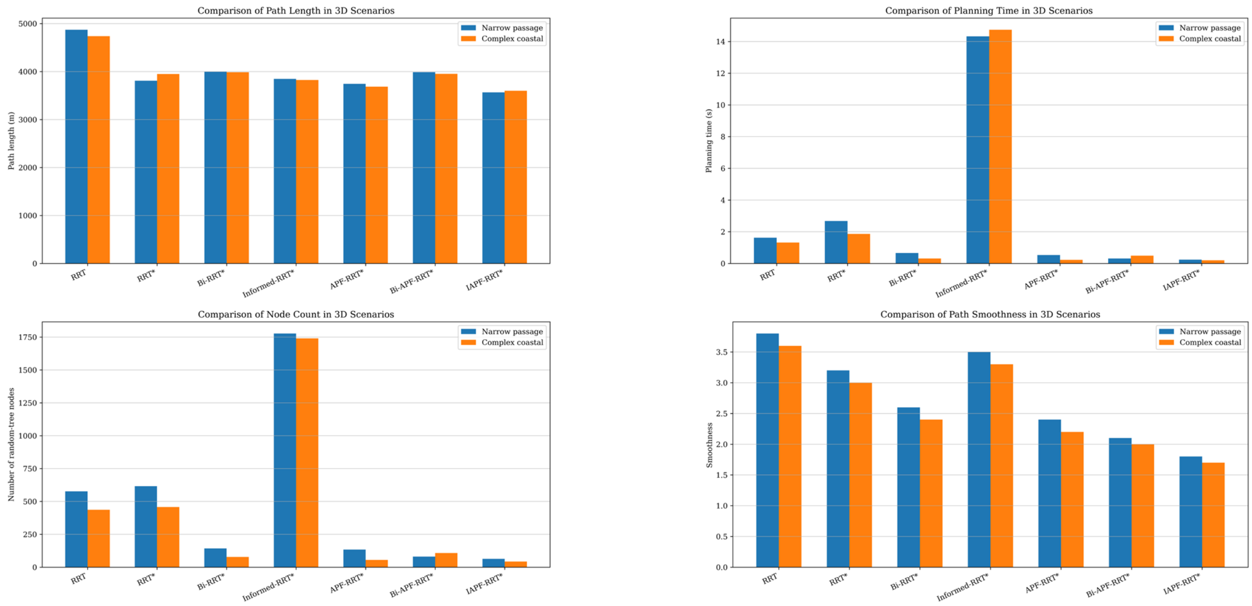

Figure 22. Comparison of 3D experimental metrics.

Table 6. Ablation study results of different modules (mean ± std over 30 runs).

Algorithm	Path Length (m)	Planning Time (s)	Number of Random-Tree Nodes	Smoothness	Success Rate [1] (%)
M1	153.53 ± 6.41	10.78 ± 1.32	302 ± 48	3.50 ± 0.24	90.00
M2	149.85 ± 5.87	3.12 ± 0.51	182 ± 30	2.68 ± 0.17	93.33
M3	150.21 ± 5.42	2.36 ± 0.39	168 ± 27	2.84 ± 0.18	96.67
M4	148.36 ± 4.83	1.69 ± 0.28	142 ± 23	2.46 ± 0.13	96.67
M5	147.88 ± 4.31	1.35 ± 0.22	135 ± 21	2.30 ± 0.10	100.00

[1] Success rate was calculated from 30 trials.

Table 7. Ablation results in dynamic obstacle scenarios (mean ± std over 30 runs).

Algorithm	Success Rate [1] (%)	Min Distance (m)	Planning Time (s)	Smoothness
M4 without dynamic avoidance	90.00	0.42 ± 0.05	1.57 ± 0.23	2.63 ± 0.16
M4 with dynamic avoidance	96.67	0.55 ± 0.06	1.74 ± 0.26	2.49 ± 0.13
M5 (full method)	100.00	0.61 ± 0.05	1.39 ± 0.21	2.30 ± 0.10

[1] Success rate was calculated from 30 trials.

The results presented in Table 6 demonstrate the contribution of each module in a complex mixed environment. Compared with the baseline RRT*, the introduction of IAPF guidance (M2) significantly improves the success rate while reducing both planning time and node expansion. However, its performance remains slightly inferior to that of APF-RRT*, indicating that the guidance mechanism alone is insufficient to fully exploit its potential. With the addition of target-biased sampling (M3), the planning time is further reduced. Meanwhile, a slight increase in path length and smoothness index is observed, suggesting that the stronger directional bias may introduce temporary exploration instability in cluttered environments. The adaptive attraction weighting (M4) further improves trajectory smoothness and robustness by effectively suppressing unnecessary oscillatory behavior during tree expansion. Finally, the full method (M5) achieves the best overall performance, outperforming APF-RRT* across all key metrics. This demonstrates that the proposed IAPF-RRT* framework effectively integrates guidance, sampling, and trajectory optimization into a unified planning strategy.

As shown in Table 7, compared with the variant without the dynamic obstacle module, the introduction of velocity-aware avoidance significantly improves the success rate and increases the minimum clearance from dynamic obstacles, while substantially reducing the collision rate. A slight increase in planning time is observed due to the additional online avoidance computations, reflecting the increased decision complexity in dynamic environments. The full method achieves the best overall performance, indicating that the dynamic obstacle avoidance module and the trajectory refinement strategy jointly enhance navigation safety and stability.

While the above simulation results and ablation analysis validate the effectiveness of the proposed method under controlled conditions, further validation in real-world environments is still necessary. Therefore, field experiments were conducted to evaluate the practical performance of the proposed approach.

4.5. Parameter Sensitivity Analysis and Practical Considerations

To evaluate the robustness and practical applicability of the proposed IAPF-RRT* framework, a parameter sensitivity analysis was conducted on key parameters, including the repulsive gain coefficient k_{rep}, the obstacle influence distance ρ_o, the step size Δd, and the initial target-biased sampling probability p_0. These parameters play a critical role in balancing exploration capability, convergence efficiency, and obstacle avoidance performance.

As shown in Figure 23a, the repulsive gain coefficient k_{rep} mainly influences obstacle avoidance behavior and node expansion. When k_{rep} is too small, the repulsive force becomes insufficient, leading to trajectories that approach obstacles too closely and potentially increasing collision risk. Conversely, excessively large values result in over-conservative avoidance, causing redundant node expansion and increased computational cost. An intermediate value achieves a balanced trade-off between safety and efficiency. Figure 23b illustrates the effect of the obstacle influence distance ρ_o. This parameter determines the spatial range of repulsive interaction. A small ρ_o delays obstacle avoidance, resulting in sharper turns and reduced smoothness, whereas a large ρ_o causes premature deviation from the optimal path and unnecessary detours. The results indicate that a moderate value yields improved trajectory smoothness while maintaining efficient exploration. In Figure 23c, the step size Δd has a direct impact on convergence efficiency and feasibility. Smaller step sizes enable finer resolution in narrow or cluttered environments, improving success rate but increasing computational cost. In contrast, larger step sizes accelerate the exploration process but may skip feasible narrow passages, leading to reduced success rates. Therefore, an appropriate step size is essential for balancing efficiency and reliability. Figure 23d presents the sensitivity to the initial sampling bias p_0, which controls the balance between random exploration and goal-directed search. A low p_0 enhances exploration capability but results in longer planning time, while a high p_0 accelerates convergence but may increase the risk of local trapping in complex environments. The results show that a moderate sampling bias achieves both high efficiency and a stable success rate. The proposed IAPF-RRT* method demonstrates stable performance over a relatively broad range of parameter values. These observations confirm that the selected parameter configuration provides a well-balanced trade-off among exploration capability, convergence efficiency, and obstacle avoidance performance, and that the method is robust to moderate parameter variations.

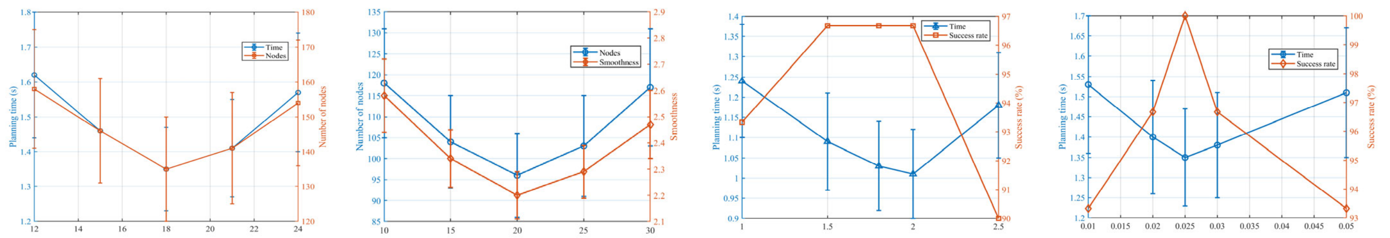

(**a**) (**b**) (**c**) (**d**)

Figure 23. Parameter sensitivity analysis of the proposed IAPF-RRT* method with respect to key parameters: (**a**) repulsive gain coefficient k_{rep}; (**b**) obstacle influence distance ρ_o; (**c**) step size Δd; (**d**) target-biased sampling probability p_0.

Based on the above sensitivity analysis, practical parameter tuning guidelines can be summarized. The repulsive parameters k_{rep} and ρ_o should be selected according to obstacle density and required safety margin, where moderate values are recommended to avoid excessive detours or insufficient obstacle avoidance. The step size Δd can be adjusted according to environmental complexity, with smaller values preferred in narrow or cluttered environments to improve feasibility, and larger values used in sparse environments to enhance computational efficiency. The initial sampling bias p_0 should be chosen to balance exploration and convergence speed, where a moderate value is generally sufficient for most scenarios.

Furthermore, a trade-off exists between planning performance and computational cost. Increasing exploration capability (e.g., smaller step size or lower sampling bias) improves success rate and path quality but leads to higher computational overhead. Conversely, stronger goal bias and larger step size reduce planning time but may degrade robustness in complex environments. Therefore, the proposed parameter configuration provides a balanced compromise between efficiency, robustness, and trajectory quality.

4.6. Field Experimental Validation in Nearshore Environments

This section presents field experiments evaluating the path planning performance of UUVs in nearshore environments. The experiment was conducted using the in-house developed "Zhihai No.2" platform, as shown in Figure 24a. The vehicle has a compact form factor (23 × 23 × 90 cm) and a lightweight structure (26 kg), enabling agile maneuvering in confined and cluttered underwater spaces. The trials were carried out in an offshore aquaculture area near Phoenix Island. During the mission, the UUV traversed the farming region while performing water-sample collection for quality assessment. The start and goal waypoints were preset at (36.00739° N, 120.30830° E) and (36.01040° N, 120.31033° E), respectively. Considering the relatively uniform water quality in this region, only one patrol point near each fish cage was required to optimize sampling efficiency and minimize redundant measurements. Accordingly, four patrol points were deployed along the route: Patrol 1 (36.00791° N, 120.30915° E), Patrol 2 (36.00836° N, 120.30951° E), Patrol 3 (36.00892° N, 120.31020° E), Patrol 4 (36.00954° N, 120.31024° E). The total navigation distance was approximately 420 m, providing adequate spatial coverage for validating the proposed algorithm in a realistic nearshore aquaculture environment. The shore-based experimental setup and monitoring station are shown in Figures 24b and 24c, respectively, enabling real-time data transmission, UUV control, and status monitoring. The far-field experimental site, an offshore aquaculture cage farm, is illustrated in Figure 24d. The UUV operation platform used during the sea trials is schematically shown in Figure 24e, including the stationary buoy for positioning, the surface vessel for command and monitoring, and a predefined desired trajectory. The path-tracking performance in the real-world application scenario is presented in Figure 25. The parameter settings used in the field experiments are largely consistent with those in the simulation. The core algorithmic parameters, including k_{att}, k_{rep}, and ρ_o, are kept unchanged to ensure methodological consistency. Only a few environment-dependent parameters are slightly adjusted. Specifically, the step size Δd is adapted to match the motion resolution of the UUV platform, the sampling bias is moderately increased to improve stability under real-world disturbances, and the maximum number of iterations is limited to satisfy real-time requirements. No extensive parameter re-tuning was performed. Therefore, the field results directly demonstrate the robustness and practical applicability of the proposed method. To mitigate the effects of environmental disturbances and experimental uncertainty, each sea trial was repeated five times under comparable conditions, and the averaged results are reported in Table 8.

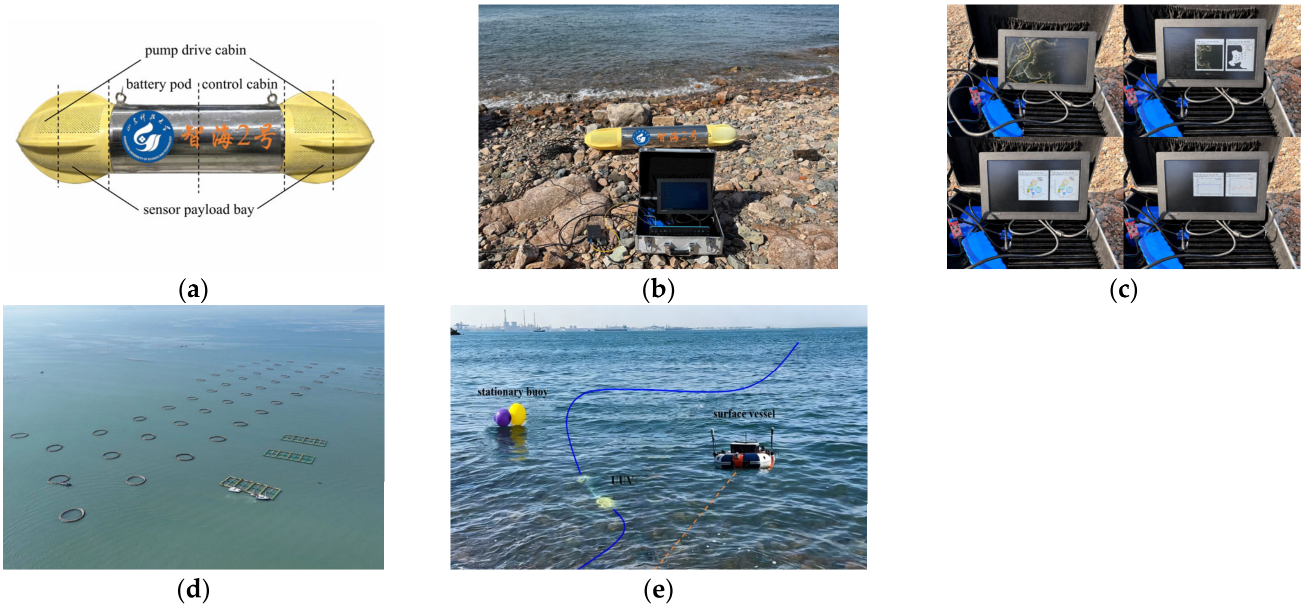

Figure 24. Real-environment experimental setup for the UUV-based aquaculture monitoring system: (**a**) the "Zhihai No.2" UUV; (**b**) shore-based experimental equipment; (**c**) shore-based monitoring and control station; (**d**) aerial view of the offshore aquaculture cage farm; (**e**) schematic of the UUV operation in the sea trial.

While simulations confirm the effectiveness of the proposed method, field experiments expose additional challenges in real underwater environments. Nearshore aquaculture areas involve complex hydrodynamic disturbances, positioning uncertainties, and irregular obstacle distributions, which introduce variability into the planning and tracking process and often degrade the performance of conventional sampling-based methods.

As shown in Figure 25 and Table 8, traditional algorithms such as RRT and RRT* are more sensitive to environmental disturbances, resulting in unstable trajectories and frequent deviations. Although the SOTA method Informed-RRT* improves sampling efficiency, it still suffers from redundant exploration in cluttered regions due to the lack of obstacle-aware guidance. APF-based methods enhance obstacle avoidance but tend to produce local oscillations under dense and dynamic conditions. In contrast, the proposed IAPF-RRT* generates more stable and smoother trajectories with reduced heading variations, leading to improved maneuverability in confined environments. It also achieves lower energy consumption, primarily due to fewer unnecessary maneuvers and reduced oscillatory motion. These results indicate that improving path smoothness is critical for enhancing both energy efficiency and operational endurance in real-world UUV applications.

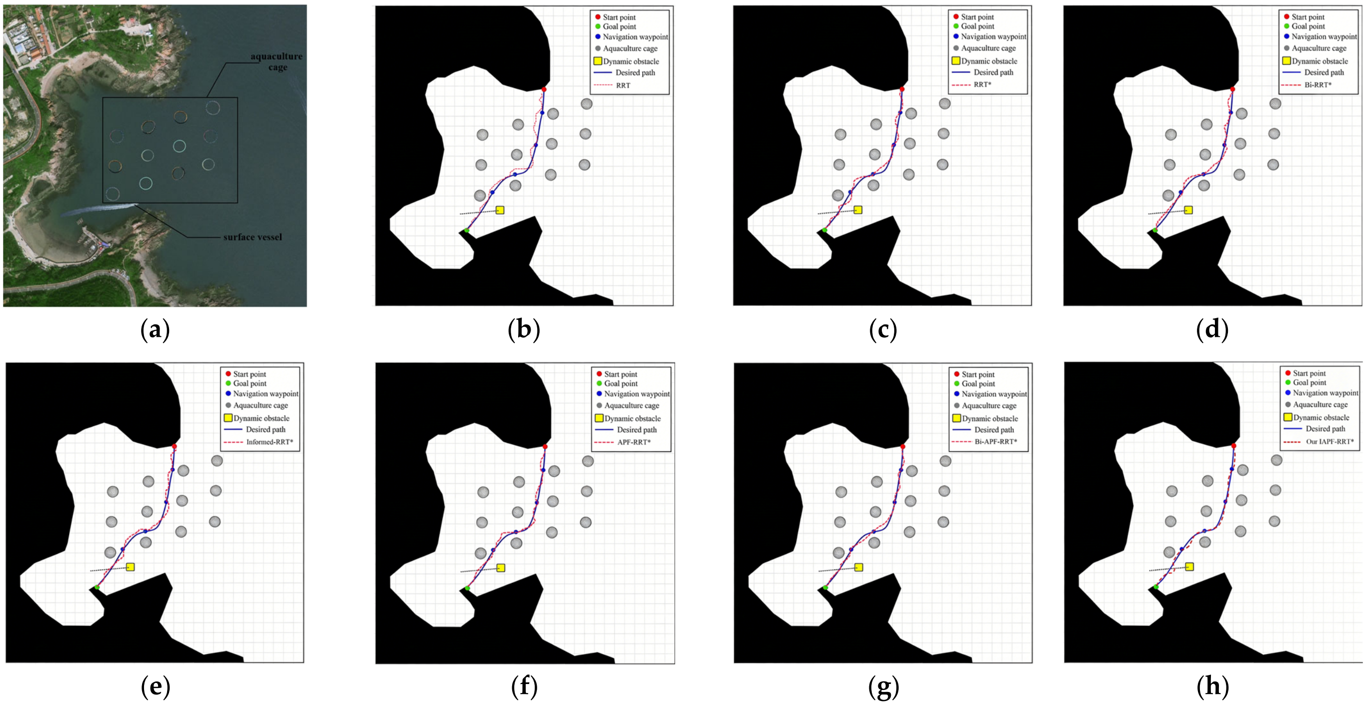

Figure 25. Real environment experimental condition: (**a**) experimental area; (**b**) RRT; (**c**) RRT*; (**d**) Bi-RRT*; (**e**) Informed-RRT*; (**f**) APF-RRT*; (**g**) Bi-APF-RRT*; (**h**) our IAPF-RRT*. In each subfigure, the grey dashed line denotes the trajectory of the dynamic obstacle.

Table 8. Real environment experimental data.

Algorithm	Path Length (m)	Navigation Time (min)	Energy Consumption (Wh)	Smoothness	Success Rate (%)
RRT	569	14.57	37.74	3.0	60
RRT*	543	14.07	35.97	2.5	60
Bi-RRT*	487	13.27	30.73	2.3	80
Informed-RRT*	468	12.83	27.05	2.4	80
APF-RRT*	455	11.80	26.50	2.1	80
Bi-APF-RRT*	432	10.50	24.80	2.0	100
Our IAPF-RRT*	427	9.72	23.33	1.7	100

4.7. Comparative Discussion and Analysis

The results from both simulations and field experiments consistently demonstrate the effectiveness of the proposed IAPF-RRT* algorithm. Compared with conventional sampling-based methods, the proposed approach reduces redundant node expansion and improves convergence efficiency across different scenarios. In terms of trajectory quality, the proposed method generates smoother and more stable paths, especially in constrained environments such as narrow passages and cluttered nearshore regions. Although a slight increase in path length is observed in some complex cases, the overall improvement in smoothness, stability, and success rate makes the method more practical for real-world applications. From a mechanism perspective, these improvements mainly come from two aspects. On the one hand, the dynamic goal-bias strategy enhances directional guidance during tree expansion, reducing unnecessary exploration. On the other hand, the improved potential field provides a more balanced interaction between attraction and repulsion, which helps suppress local oscillations and improves path continuity. The field experiments further confirm that these advantages are maintained in real-world environments. In particular, smoother trajectories contribute to reduced control effort and energy consumption, which is critical for extending UUV mission duration. Moreover, the improved robustness and higher success rate enhance the reliability of autonomous navigation in cluttered aquaculture environments, demonstrating the practical applicability of the proposed approach. Compared with optimization-based and learning-based methods, the proposed approach does not rely on global trajectory optimization or large-scale training data, making it more suitable for real-time deployment in uncertain nearshore environments.

In practical marine environments, localization is subject to noise and latency. To emulate these effects, Gaussian noise is introduced into the UUV state and obstacle positions during simulation. The proposed IAPF-RRT* maintains stable performance under moderate noise levels, benefiting from its sampling-based nature and reactive re-planning mechanism. The continuous re-planning strategy mitigates the impact of sensor latency by updating trajectories based on the latest observations, while performance may degrade under severe uncertainty or significant delays.

It is also important to note that the integration of APF-based guidance introduces a directional bias into the sampling and node expansion processes, which may affect the strict asymptotic optimality guarantees of the original RRT* algorithm. Specifically, the uniform sampling assumption required for theoretical optimality is partially relaxed. However, the proposed method retains sufficient stochastic exploration capability and does not eliminate randomness in the sampling process. More importantly, in practical finite-time planning scenarios, the proposed approach achieves significantly improved convergence efficiency, reduced redundant exploration, and enhanced trajectory quality. Therefore, a trade-off exists between strict asymptotic optimality and practical performance, where the proposed method prioritizes efficiency, robustness, and smoothness, which are more critical for real-world UUV applications.

Although the proposed IAPF-RRT* framework is developed and validated for UUV operations in nearshore environments, its underlying principles are not limited to underwater applications and can be extended to other robotic platforms, such as unmanned aerial vehicles (UAVs) and unmanned ground vehicles (UGVs). The sampling-based planning framework combined with potential field guidance is largely independent of specific vehicle dynamics, and the target-biased sampling strategy and adaptive guidance mechanism can be applied to enhance convergence efficiency and planning robustness in various environments.

However, when extending the proposed method to other platforms, several challenges arise. Differences in dynamic constraints, sensing modalities, and environmental characteristics may influence trajectory feasibility and decision-making processes. For example, UAVs operate in fully three-dimensional spaces with high maneuverability, while UGVs are constrained by nonholonomic motion and terrain conditions. These differences require appropriate adaptations to motion models and feasibility constraints.

In addition, several limitations of the proposed method should be acknowledged. First, the current framework mainly focuses on geometric path planning and does not explicitly incorporate full UUV dynamic constraints or complex hydrodynamic effects. Second, although moderate localization noise and sensor latency are considered, the method has not been systematically evaluated under severe uncertainty conditions. Third, while the parameter settings exhibit good robustness, they may still require adjustment in highly heterogeneous environments. These limitations do not undermine the effectiveness of the proposed framework but indicate directions for further improvement. These limitations indicate several directions for future work, including uncertainty-aware planning, adaptive parameter tuning, and tighter perception–planning integration.

https://doi.org/10.3390/jmse14090851

5. Conclusions

This paper proposes an IAPF-RRT* framework for global path-planning of UUVs in complex nearshore environments. By integrating the IAPF model into the RRT* framework, the proposed method provides dynamic guidance during sampling and node expansion, thereby enhancing goal-directed exploration and accelerating convergence. To overcome the limitations of existing SOTA methods, a distance-adjusted repulsive potential is introduced to ensure global goal reachability, while a relative-velocity-based avoidance strategy enables adaptive responses to dynamic obstacles. In addition, a target-biased sampling mechanism and a weight-adaptive attraction strategy are incorporated to improve exploration efficiency and suppress redundant node expansion. A NURBS-based path refinement module is further employed to enhance trajectory smoothness and curvature continuity. Extensive simulations and real-world experiments demonstrate that the proposed method consistently outperforms representative state-of-the-art approaches, achieving significant reductions in planning time, node expansion, and energy consumption, while maintaining high success rates across diverse scenarios. More importantly, the results reveal that effective coordination between global exploration and local guidance is critical for improving both convergence efficiency and path stability in complex environments. In particular, suppressing redundant exploration and reducing trajectory oscillations are key factors for enhancing energy efficiency and operational reliability in real-world UUV applications. These findings indicate that the proposed mechanism-level integration strategy provides a general and effective solution for improving sampling-based path planning methods. The framework not only advances the state of the art but also offers strong practical applicability for autonomous navigation in nearshore and aquaculture environments.

Future work will focus on enhancing robustness under uncertain and dynamic nearshore conditions by incorporating uncertainty-aware planning (e.g., probabilistic constraints). In addition, learning-based strategies will be explored for adaptive parameter tuning and decision-making. The framework will also be extended by integrating perception modules (e.g., acoustic sensing and polarization vision) to achieve tighter perception–planning coupling and improved system autonomy. These directions aim to further enhance the robustness, adaptability, and autonomy of UUV navigation in complex nearshore environments.

Author Contributions: Methodology, X.F.; Software, X.F.; Validation, F.K. and Z.C.; Data curation, F.K., Z.C. and Y.G.; Writing—original draft, X.F.; Writing—review and editing, Y.G. and X.F.; Supervision, Y.G. All authors have read and agreed to the published version of the manuscript.

Funding: This work received partial financial support from the Shandong Provincial Natural Science Foundation under Grant ZR2024QF085, and from the National Natural Science Foundation of China through Grants 62401172 and 61471269, and the Presidents of Universities in Qingdao West Coast New Area Special Foundation for the project on Research and Application of Unmanned Equipment Systems for Key Technologies in Mariculture Farms under Grant GXXZJJ202302.

Data Availability Statement: The data presented in this study are available upon request from the corresponding author due to data management requirements of the funded project.

Acknowledgments: ChatGPT (OpenAI, GPT-5) was used for language polishing and grammar correction of the manuscript. All authors have reviewed and revised the content and take full responsibility for the accuracy and integrity of the work.

Conflicts of Interest: The authors declare that the research was conducted in the absence of any commercial or financial relationships that could be construed as a potential conflict of interest.

References

1. Guo, X.; Zhao, D.; Fan, T.; Long, F.; Fang, C.; Long, Y. Autonomous underwater vehicle path planning based on improved salp swarm algorithm. *J. Mar. Sci. Eng.* **2024**, *12*, 1446. [CrossRef]
2. Zhang, X.; Hao, X.; Zhang, L.; Liu, L.; Zhang, S.; Ren, R. Multi-autonomous underwater vehicle full-coverage path planning in complex marine environments. *J. Mar. Sci. Eng.* **2024**, *12*, 1276. [CrossRef]
3. Liu, Y.; Sun, J.; Li, G.; Xu, X. AUV online path planning strategy based on sectorial gridded detection area. *J. Mar. Sci. Eng.* **2025**, *13*, 443. [CrossRef]
4. Zhou, S.; Wang, Z.; Li, L.; Li, H. Research on multi-target path planning for UUV based on estimated path cost. *J. Mar. Sci. Eng.* **2023**, *11*, 1582. [CrossRef]
5. Zhang, Z.; Lin, M.; Li, D.; Wu, R.; Lin, R.; Yang, C. An AUV-enabled dockable platform for long-term dynamic and static monitoring of marine pastures. *IEEE J. Ocean. Eng.* **2025**, *50*, 276–293. [CrossRef]
6. Li, D.; Wang, P.; Du, L. Path planning technologies for autonomous underwater vehicles: A review. *IEEE Access* **2019**, *7*, 9745–9768. [CrossRef]
7. Lai, Y.; Li, Y.; Xu, Z.; Han, J.; Kang, W.; Liu, Z. A review on path planning for autonomous underwater vehicles: From models, classical methods, and learning-based intelligence perspectives. *J. Field Robot.* **2025**, *43*, 2366–2389. [CrossRef]
8. Ru, J.; Yu, S.; Wu, H.; Li, Y.; Wu, C.; Jia, Z.; Xu, H. A multi-AUV path planning system based on omni-directional sensing ability. *J. Mar. Sci. Eng.* **2021**, *9*, 806. [CrossRef]
9. Li, Y.; Ma, T.; Chen, P.; Jiang, Y.; Wang, R.; Zhang, Q. Autonomous underwater vehicle optimal path planning method for seabed terrain matching navigation. *Ocean Eng.* **2017**, *133*, 107–115. [CrossRef]
10. Chen, Z.; Yan, J.; Huang, R.; Gao, Y.; Peng, X.; Yuan, W. Path planning for autonomous underwater (AUVs) vehicles considering the influences and constraints of ocean currents. *Drones* **2024**, *8*, 348. [CrossRef]
11. Khatib, O. Real-time obstacle avoidance for manipulators and mobile robots. *Int. J. Robot. Res.* **1986**, *5*, 90–98. [CrossRef]
12. Fan, X.; Guo, Y.; Liu, H.; Wei, B.; Lyu, W. Improved artificial potential field method applied for AUV path planning. *Math. Probl. Eng.* **2020**, *2020*, 6523158. [CrossRef]
13. Xing, T.; Wang, X.; Ding, K.; Ni, K.; Zhou, Q. Improved artificial potential field algorithm assisted by multisource data for AUV path planning. *Sensors* **2023**, *23*, 6680. [CrossRef]
14. Zhao, Z.; Zhang, Y.; Feng, X.; Jiang, C.; Su, W.; Hu, Q. A dynamic velocity potential field method for multi-AUV cooperative hunting tasks. *Ocean Eng.* **2024**, *292*, 116813. [CrossRef]
15. Sun, M. The path planning algorithm for UUV based on the fusion of grid obstacles of artificial potential field. *Ocean Eng.* **2024**, *294*, 117008. [CrossRef]
16. Orozco-Rosas, U.; Montiel, O.; Sepúlveda, R. Mobile robot path planning using membrane evolutionary artificial potential field. *Appl. Soft Comput.* **2019**, *77*, 236–251. [CrossRef]
17. Orozco-Rosas, U.; Picos, K.; Pantrigo, J.J.; Montemayor, A.S.; Cuesta-Infante, A. Mobile robot path planning using a QAPF learning algorithm for known and unknown environments. *IEEE Access* **2022**, *10*, 84648–84663. [CrossRef]
18. Meng, R.; Sun, A.; Wu, Z.; Du, X.; Meng, Y. 3D smooth path planning of AUV based on improved ant colony optimization considering heading switching pressure. *Sci. Rep.* **2023**, *13*, 12348. [CrossRef] [PubMed]
19. Meng, R.; Cheng, X.; Wu, Z. Improved ant colony optimization for safe path planning of AUV. *Heliyon* **2024**, *10*, e27645. [CrossRef]
20. Hao, K.; Zhao, J.; Li, Z.; Liu, Y.; Zhao, L. Dynamic path planning of a three-dimensional underwater AUV based on an adaptive genetic algorithm. *Ocean Eng.* **2022**, *266*, 112814. [CrossRef]
21. Yin, L.; Yan, Z.; Tian, Q.; Li, H.; Xu, J. A novel robust algorithm for path planning of multiple autonomous underwater vehicles in the environment with ocean currents. *Ocean Eng.* **2024**, *312*, 119260. [CrossRef]
22. Yang, B.; Yao, L.; Chen, L.; Luo, W. Path planning of an underwater vehicle by CFD numerical simulation combined with a migration-based genetic algorithm. *J. Mar. Sci. Eng.* **2025**, *13*, 482. [CrossRef]
23. LaValle, S.M.; Kuffner, J.J. Rapidly-Exploring Random Trees: Progress and Prospects. In *Algorithmic and Computational Robotics*; CRC Press: Boca Raton, FL, USA, 2001; pp. 293–308.
24. Jamieson, J.; Biggs, J. Path planning on SE(3) for autonomous underwater vehicles using the rapidly-exploring random tree method. In Proceedings of the IFAC World Congress, Cape Town, South Africa, 24–29 August 2014; pp. 454–459.
25. Hernández, E.; Balachandran, R.; Ridao, P. On-line 3D path planning for close-proximity surveying with autonomous underwater vehicles. In Proceedings of the 10th IFAC Conference on Control Applications in Marine Systems, Osaka, Japan, 18–20 September 2015; pp. 91–96.
26. Karaman, S.; Frazzoli, E. Sampling-based algorithms for optimal motion planning. *Int. J. Robot. Res.* **2011**, *30*, 846–894. [CrossRef]
27. Li, Y.; Sun, Z.; Zhang, H. Three-dimensional path planning for autonomous underwater vehicles in ocean environments. *Ocean Eng.* **2023**, *266*, 113042.

28. Gammell, J.D.; Srinivasa, S.S.; Barfoot, T.D. Informed RRT*: Optimal sampling-based path planning focused via direct sampling of an admissible ellipsoidal heuristic. In Proceedings of the 2014 IEEE/RSJ International Conference on Intelligent Robots and Systems, Chicago, IL, USA, 14–18 September 2014; pp. 2997–3004.
29. Zhao, Y.; Li, Q.; Wang, M. Underwater 3D path planning for autonomous underwater vehicles in ocean currents based on informed RRT*. *J. Intell. Robot. Syst.* **2025**, *109*, 116. [CrossRef]
30. Jordan, M.; Perez, A. *Optimal Bidirectional Rapidly-Exploring Random Trees*; Massachusetts Institute of Technology: Cambridge, MA, USA, 2013.
31. Gao, X.; Chen, Y.; Wang, L. Underwater vehicle path planning based on bidirectional RRT*. *Appl. Sci.* **2024**, *14*, 947. [CrossRef]
32. Ge, Z.; Liu, Y.; Zhang, Q. RRT*-enhanced long-horizon path planning for autonomous underwater vehicles. *Knowl. Based Syst.* **2025**, *286*, 110646.
33. Feng, H.; Hu, Q.; Zhao, Z.; Feng, X. Smooth path planning under maximum curvature constraints for autonomous underwater vehicles based on RRT* with B-spline curves. *Eng. Appl. Artif. Intell.* **2024**, *133*, 108583. [CrossRef]
34. Urmson, C.; Simmons, R. Approaches for heuristically biasing RRT growth. In Proceedings of the 2003 IEEE/RSJ International Conference on Intelligent Robots and Systems (IROS 2003) (Cat. No.03CH37453), Las Vegas, NV, USA, 27–31 October 2003; pp. 1178–1183.
35. Lu, Y.; Wu, A.; Chen, Q.; Wang, Y. An improved UAV path planning method based on RRT-APF hybrid strategy. In Proceedings of the 2020 5th International Conference on Automation, Control and Robotics Engineering (CACRE), Dalian, China, 19–20 September 2020; pp. 81–86.
36. Hong, L.; Song, C.; Yang, P.; Cui, W. Two-layer path planner for AUVs based on the improved AAF-RRT algorithm. *J. Mar. Sci. Appl.* **2022**, *21*, 102–115. [CrossRef]
37. Zhu, J.; Zhao, S.; Zhao, R. Path planning for autonomous underwater vehicle based on artificial potential field and modified RRT. In Proceedings of the 2021 International Conference on Computer, Control and Robotics (ICCCR), Shanghai, China, 8–10 January 2021; pp. 21–25.
38. Zhang, B.; Su, Y.; Sun, S.; Luo, W.; Huang, Q. Hybrid path planning algorithm for underactuated autonomous underwater vehicles based on RRT* and artificial potential field. *Sci. Rep.* **2025**, *15*, 28493. [CrossRef]
39. Xie, C.; Liu, Y.; Wang, Z. An AUV path planning method based on improved APF-RRT. In Proceedings of the IEEE International Conference on Mechatronics and Automation (ICMA), Harbin, China, 6–9 August 2023; pp. 1–6.
40. Fan, J.; Chen, X.; Liang, X. UAV trajectory planning based on bi-directional APF-RRT* algorithm with goal-biased. *Expert Syst. Appl.* **2023**, *213*, 119137. [CrossRef]

Disclaimer/Publisher's Note: The statements, opinions and data contained in all publications are solely those of the individual author(s) and contributor(s) and not of MDPI and/or the editor(s). MDPI and/or the editor(s) disclaim responsibility for any injury to people or property resulting from any ideas, methods, instructions or products referred to in the content.